IMPROVING AND AUGMENTING THE ANM MODEL FOR

THREE-DIMENSIONAL VIRTUAL CONCRETE

by

Stephen Thomas

A thesis

submitted in partial fulfillment

of the requirements for the degree of

Master of Science in Materials Science and Engineering

Boise State University

August 2018

BOISE STATE UNIVERSITY GRADUATE COLLEGE

DEFENSE COMMITTEE AND FINAL READING APPROVALS

of the thesis submitted by

Stephen Thomas

Thesis Title: Improving and Augmenting the Anm Model for Three-Dimensional Virtual Concrete

Date of Final Oral Examination: 07 March 2017

The following individuals read and discussed the thesis submitted by student Stephen Thomas, and they evaluated his presentation and response to questions during the final oral examination. They found that the student passed the final oral examination.

Yang Lu, Ph.D.   Co-Chair, Supervisory Committee

Janet Callahan, Ph.D.   Co- Chair, Supervisory Committee

Peter Mullner, Ph.D.   Member, Supervisory Committee

The final reading approval of the thesis was granted by Yang Lu, Ph.D., Chair of the Supervisory Committee. The thesis was approved by the Graduate College.

DEDICATION

To my wife Anuya and my children Thomas and Mathew without whom this thesis would have been much less close to my heart.

ACKNOWLEDGEMENTS

ABSTRACT

The Anm model used for creating virtual concrete consisting of irregular shapes has been improved by integrating two existing algorithms: the extent overlap box (EOB) method for detecting contact between two irregular shapes and the uniform thickness shell algorithm. The EOB method has been compared with the previously used Newton-Raphson method and shown to be able to detect inter-particle contact with better accuracy and with less computational cost. Two parameters that define the balance between accuracy and performance of the EOB method have been identified and studied. The uniform thickness shell has been used to specify the minimum inter-particle distance in the 3D model of irregular shaped particles. A clear relation between shell thickness and packing density has been established through a series of simulations. To further improve the performance of the Anm model, the performance bottlenecks in the code have been identified and data parallelism has been introduced with minimal amount of code change. Another variation of the Anm model has been explored where the uniform thickness shell overlaps with other uniform thickness shells and other particles. The overlapping uniform thickness shell model is representative of microstructures such as the interfacial transition zone (ITZ) present in concrete. Studying such processes that depend on the Euclidian distance from the particle surface in three dimensions can be challenging. A new method for obtaining two dimensional slices of this model has been developed and resultant images showing the spatial distribution of the different phases are analyzed. It has been observed that the apparent thickness of the shell in the 2D slices

can be larger than the prescribed normal distance from the particle surface and this is dependent on the angle between the slice and the particle surface normal. The 2D analysis has been shown to be useful to explain surface features observed in actual slices of concrete samples. The "wall effect" observed in the Anm model (and real concrete) is characterized with a radial distribution function utilizing the 2D slicing feature and the methods for performing this characterization is developed.

TABLE OF CONTENTS

LIST OF TABLES

LIST OF FIGURES

LIST OF ABBREVIATIONS

EOB	Extent Overlap Box
ITZ	Interfacial Transition Zone
API	Application Programming Interface
PSD	Particle Size Distribution
PD	Packing Density
NR	Newton-Raphson
N_{ext}	The number of equally spaced polar and azimuthal angles to scan the particle to find the six extrema of the EOB.
N_{box}	The number of equally spaced polar and azimuthal angles to scan the EOB to detect contact of particles.
PPL	Microsoft Parallel Patterns Library
MPI	Message Passing Interface

CHAPTER ONE: INTRODUCTION

This chapter consists of three sections. The first section describes the background and the motivation of this research. The second section describes the state of the art of this research area. In the third section, the research objectives are presented.

1.1 Background

Concrete is the most widely used man-made material today and humans used it as early as the ancient Greeks (Jackson *et al.*, 2011). However, there is still much to be elucidated at the micro and nano scale of this material. At the nanoscale, the major phase of cement paste, the calcium-silicate-hydrate (C-S-H) phase is considered a heterogeneous material. The study of C-S-H is an active area of research (Pellenq *et al.*, 2009; Masoero *et al.*, 2014). At the microscale, concrete is a heterogeneous material with either two or three phases. The two-phase model considers mortar as the matrix and coarse aggregates as the inclusions. The three-phase model considers cement paste as the matrix with both fine aggregates (sand) and coarse aggregates as the inclusions.

A true understanding of concrete requires a multiscale approach. Robust predictive computer models are needed to be able to progress concrete design further and reliably predict the physical properties. The motivations for such a capability include the variability in material sources, mixing processes, and the time dependent evolution of the properties of concrete. Mechanical properties are of primary interest for concrete because of its extensive use as a structural material. The mechanical properties of interest are the linear elastic properties which govern the behavior at small strains, the viscoelastic

properties that govern the long-term deflections and the properties associated with failure. Even for linear elastic behavior of cementitious materials, theoretically predicting the composite elastic modulus tensor is non-trivial (Haecker *et al.*, 2005).

Irrespective of which type of physical property is of concern and the type of simulation method used, one of the important constituents of the microscale model is the microstructure. The microstructural model considers details such as phase volume fractions, particle gradation and porosity. Software packages such as CEMHYD3D (Bentz, 1997) and the Virtual Cement and Concrete Testing Laboratory (VCCTL) (Bentz *et al.*, 2006; Bullard and Garboczi, 2006) use an initial microstructure as the input to predict various properties of cement and concrete. These predictions rely heavily on the accuracy of the input model. These software packages consider three dimensional models since unlike phase volume fractions which are same in two and three dimensions, connectivity and percolation of phases are different in two and three dimensions. Due to these factors, mechanical and transport behavior are predicted more accurately using three dimensional models.

1.2 State of the art

In general, the microstructural model can be obtained either by imaging a physical specimen of concrete using techniques such as X-ray computed tomography (CT) or by virtually building the model using a computer program. The former method has the advantage of being the exact representation of the actual physical sample. However, it must be noted that some information is usually lost during digitization while trying to reduce noise and due to limitations in resolution. Though not an exact replica of actual physical samples, the models generated using the latter method provide the flexibility of

varying particle size distribution (PSD) and packing density (PD) which are key factors describing the microstructure and have real-world implications. For instance, a less dense packing of aggregates requires more cement paste to fill in the voids, thereby increasing the cost of the concrete mix.

Beyond the virtual model affecting the flexibility of varying PSD and PD, the virtual model also is computationally more efficient. The CT scanned models are usually voxel based 3D volumes where the entire volume of the specimen, including the matrix and inclusions must be digitally stored. In contrast, virtual microstructure models usually store just the positions, sizes, orientation, and the shape information of the inclusions. The hard-core soft-shell model (Bentz, Garboczi and Snyder, 1999) is an example of such a model. It is apparent that the shape information is trivial to obtain and store for regular shapes such as spheres and ellipsoids. Typically, the virtual models randomly pack the shapes into a given volume while making sure that the shapes do not overlap each other when the shapes represent inclusions such as aggregates. Again, it is obvious that functions for detecting contact are readily available for regular shapes.

The microstructural models using regular shapes (Amirjanov and Sobolev, 2008) have the advantages of both computational efficiency and ease of implementation. However, the particle shape becomes important to consider for situations such as fresh concrete rheology, early age mechanical properties and fracture. Aggregate shape is also known to influence the workability of concrete (Quiroga and Fowler, 2004). Due to the lack of readily available mathematical methods to represent irregular shaped particles, most of the microstructural models relied on regular shapes until the recent development of the method that extracts shape of individual real aggregates from 3D volumes of multi-

aggregate samples followed by fitting the extracted shapes to spherical harmonic

functions (Garboczi, 2002).

The starting point for this method is a 3D volume such as shown in Fig. 1.1,

acquired using X-ray CT scanning. The black voxels represent the matrix and unresolved

fine aggregates whereas the white pixels represent the coarse aggregates. The individual

particle voxels are then identified using a procedure called the "burning algorithm"

(Garboczi, 2002) and extracted for spherical harmonic analysis.
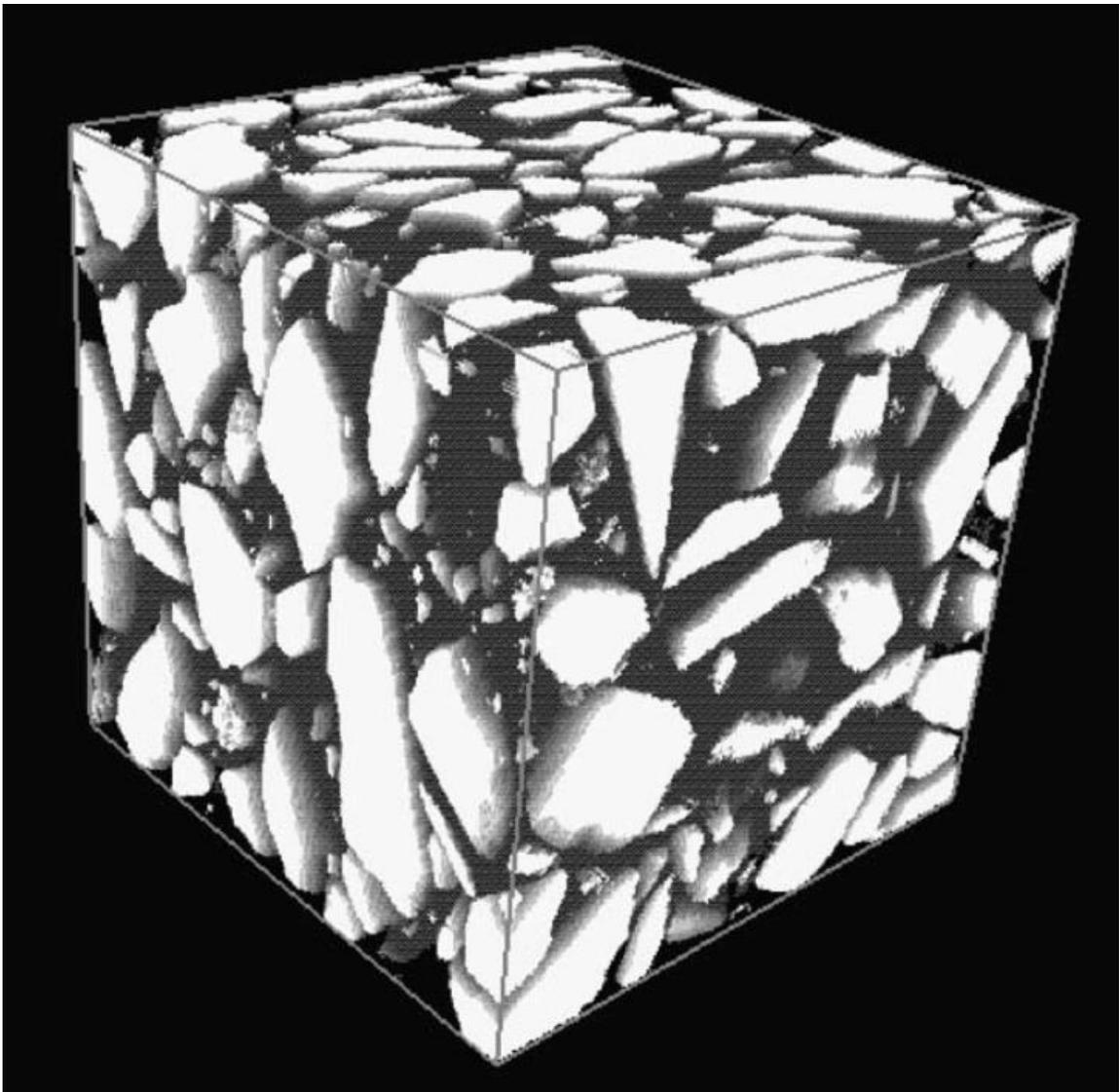
Fig. 1.1   3D volume of a multi aggregate sample obtained by X-ray CT scanning. Reproduced from (Garboczi, 2002)

Next, the distance $R(\theta_i, \phi_i)$ from the center of mass of individual particles to the surface along a finite number of angles (θ_i, ϕ_i) in the polar coordinate system are numerically obtained and recorded in a database. Once the surface points $R(\theta_i, \phi_i)$ of a particle are identified, spherical harmonic analysis is applied to obtain a function for the shape as shown in Eq. 1.1. Here $r(\theta, \phi)$ is known from $R(\theta_i, \phi_i)$ and $Y_n^m(\theta, \phi)$ are a set of predefined functions known as the spherical harmonic functions as shown in Eq. 1.2 where P_n^m is a set of orthogonal Legendre polynomials. Spherical harmonic analysis is the 3D equivalent of Fourier analysis in 2D and the spherical harmonic functions are readily available from software packages such as the Boost C++ library (Schaling, 2014).

$$r(\theta, \phi) = \sum_{n=0}^{\infty} \sum_{m=-n}^{n} a_{nm} Y_n^m(\theta, \phi). \qquad 1.1$$

$$Y_n^m(\theta, \phi) = \sqrt{\left(\frac{(2n+1)(n-m)!}{4\pi(n+m)!} \right)} P_n^m(\cos(\theta)) e^{im\phi} \qquad 1.2$$

The coefficients a_{nm} are obtained for each particle by solving Eq. 1.1 for a finite value of n. Larger values of n gives a better approximation of the original shape. The error in approximation has been shown (Garboczi, 2002) to be negligible above n=12 for the aggregate shape shown in Fig. 1.2 which depicts the aggregate shape in voxel representation (top) and spherical harmonic expansion reconstruction (below). Spherical harmonic expansion coefficients have been determined for particles of various sizes, shapes and sources (Garboczi, 2011; Garboczi and Bullard, 2013). This method has a restriction that limits its usage to "star-shaped" particles which implies that a line passing through the center of mass will intersect the surface only two times. A violation of the star shape will be when the irregular shaped aggregate has an air void within it.
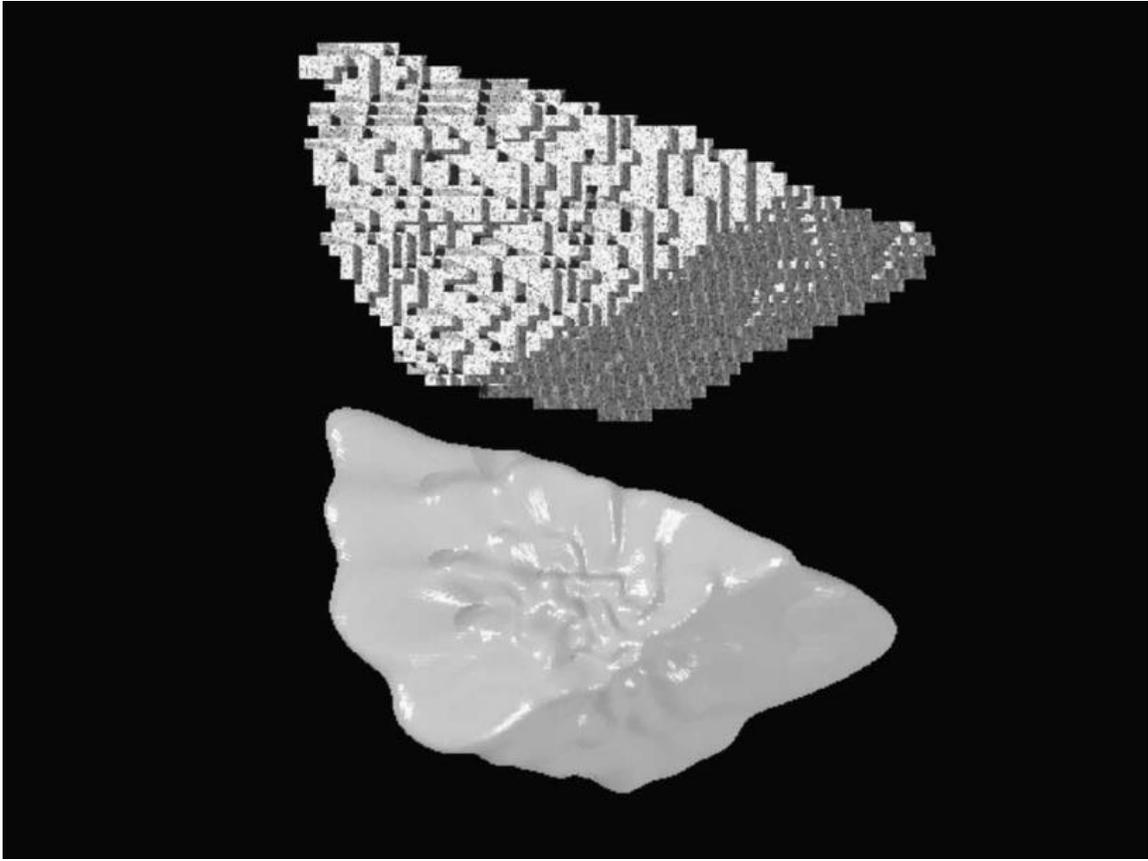
Fig. 1.2 **Aggregate shape in voxel representation (top) and spherical harmonic expansion reconstruction (below). Reproduced from (Garboczi, 2002)**

The idea of mathematically representing irregular shapes and the ability to compute geometrical properties and manipulate the shape have been applied in the recently developed material mesostructure model called the ***Anm model*** (Qian, 2012; Qian *et al.*, 2014). The Anm model introduces a framework for randomly packing a cubic volume with the irregular shapes. The input for the model includes the dimensions of the packing volume, desired packing density, number of sieves, volume density of each sieve and particle database to use for each sieve. Other important parameters include the periodicity of the boundary, number of random positions, sizes, orientations and shapes to use while randomly placing a single particle. Fig. 1.3 illustrates the algorithm used to randomly pack the particles.
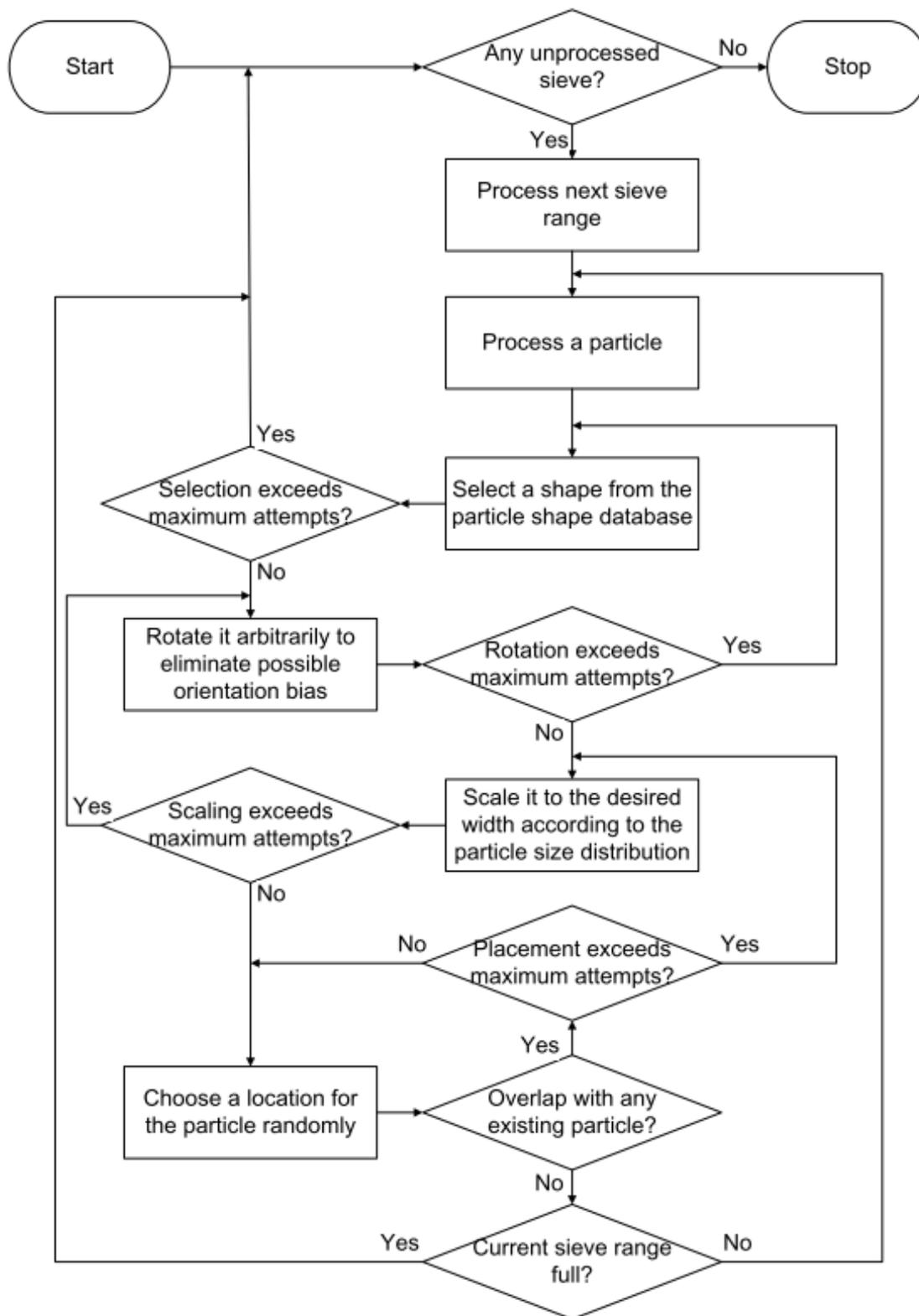
Fig. 1.3. **Flow chart illustrating the packing algorithm used by the Anm model. Reproduced from (Qian, 2012)**

One of the most critical and time consuming steps in this algorithm is the one where the placed particle is checked for overlap with any existing particles in the packed volume. In practice, not all the existing particles are checked for contact. The volume is logically divided into spatial bins and each particle being placed is assigned a bin and the overlap check is only performed on particles that belong to the bin where the new particle is being placed. The method used by the Anm model to detect contact between two particles can be understood through a sphere contact problem illustrated in Fig. 1.4.
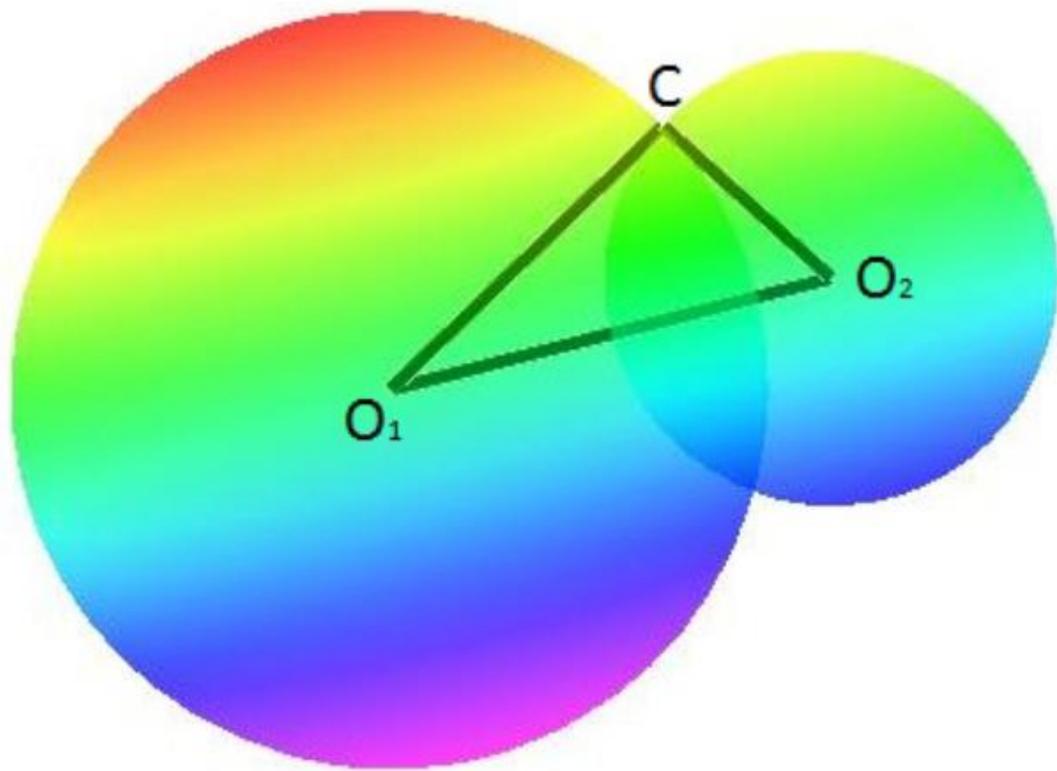
Fig. 1.4.   2D contact problem involving two circles. Reproduced from (Qian, 2012)

Here the center of mass of sphere 1 and sphere 2 are $O_1(x_1, y_1, z_1)$ and $O_2(x_2, y_2, z_2)$ and a contact point common to the two circles is $C(x_c, y_c, z_c)$. The Cartesian coordinates for the contact point $C(x_c, y_c, z_c)$ can be written in terms of the

polar coordinates of each sphere with their center of masses taken as the origins as shown in Eq. 1.3 and 1.4 where r_1 and r_2 are equivalent to the line segments O_1C and O_2C in Fig. 1.4.

$$\begin{cases} x_c = x_1 + r_1(\theta_1, \phi_1) \sin\theta_1 \cos\phi_1 \\ y_c = y_1 + r_1(\theta_1, \phi_1) \sin\theta_1 \sin\phi_1 \\ \quad z_c = z_1 + r_1(\theta_1, \phi_1) \cos\theta_1 \end{cases} \qquad 1.3$$

$$\begin{cases} x_c = x_2 + r_2(\theta_2, \phi_2) \sin\theta_2 \cos\phi_2 \\ y_c = y_2 + r_2(\theta_2, \phi_2) \sin\theta_2 \sin\phi_2 \\ \quad z_c = z_2 + r_2(\theta_2, \phi_2) \cos\theta_2 \end{cases} \qquad 1.4$$

Equating Eq. 1.3 and 1.4, a system of equations Eq. 1.5 is obtained which can be solved to obtain the unknowns $\theta_1, \phi_1, \theta_2, \phi_2$.

$$\begin{cases} x_1 + r_1(\theta_1, \phi_1) \sin\theta_1 \cos\phi_1 = x_2 + r_2(\theta_2, \phi_2) \sin\theta_2 \cos\phi_2 \\ y_1 + r_1(\theta_1, \phi_1) \sin\theta_1 \sin\phi_1 = y_2 + r_2(\theta_2, \phi_2) \sin\theta_2 \sin\phi_2 \\ \quad z_1 + r_1(\theta_1, \phi_1) \cos\theta_1 = z_2 + r_2(\theta_2, \phi_2) \cos\theta_2 \end{cases} \qquad 1.5$$

Since there are four unknowns in three equations, one of the unknowns (e.g. ϕ_1) is assumed to have a value within its allowed range ($0 \leq \theta \leq \pi, 0 \leq \phi \leq 2\pi$) and the other unknowns are then solved for using the Newton-Raphson iteration method. If a solution is obtained, the contact point exists and the two spheres are established as overlapping spheres. If a solution is not found, the two spheres are assumed to be non-overlapping spheres. The same procedure is applicable to irregular shapes. A new method (Garboczi and Bullard, 2013) that detects overlaps more efficiently was developed later using the idea of the extent overlap box (EOB). This approach relies on first detecting a bounding box called the "extent box" for each of the two particles for which overlap detection is desired. The *bounding box finding algorithm* scans the six extremum points of the irregular shape by scanning a finite number of angles within the range. A

parameter called N_{ext} determines the coarseness of this scanning and hence accuracy of the bounding box. It was found that an N_{ext} value of 40 was sufficient to reduce the error percent to less than 1% (Garboczi and Bullard, 2013). This method then checks whether the two bounding boxes intersect simply by checking their vertices. If the bounding boxes do not intersect, the EOB does not exist and the particles do not overlap. However, if an EOB exists, there is a possibility for overlap between the particles inside the EOB. This search algorithm is computationally more efficient than the Newton-Raphson iteration method used previously because it needs to scan only a sub-interval of the polar (ϕ) and azimuthal (θ) angles which are within the bounds of the EOB. Like the parameter N_{ext} which controls the resolution of the extent box scan, a parameter called N_{box} controls the resolution with which the EOB is scanned for contact. Fig. 1.5 shows examples of two particles overlapping(left) and not overlapping(right) within the EOB.
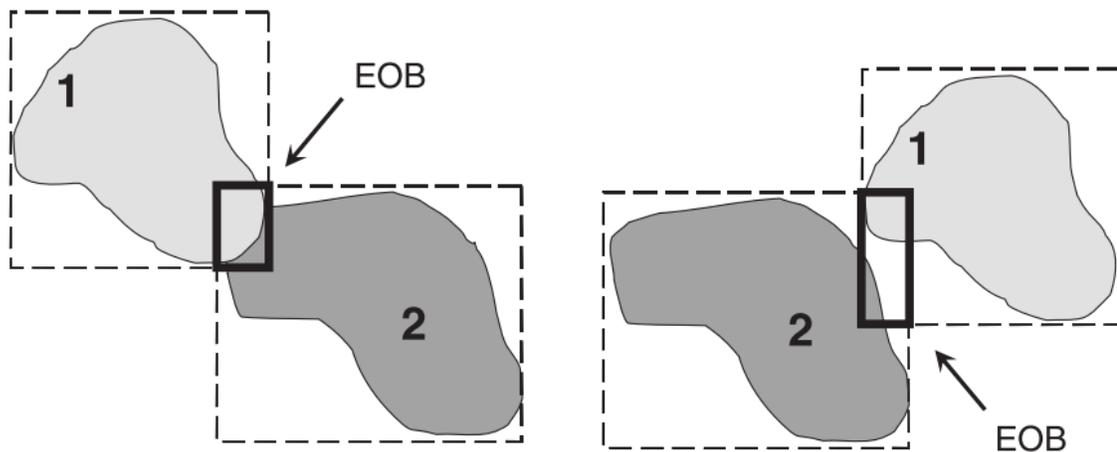
Fig. 1.5. **2D schematic showing particles overlapping(left) and not overlapping(right) within the EOB. Reprinted from (Garboczi and Bullard, 2013)**
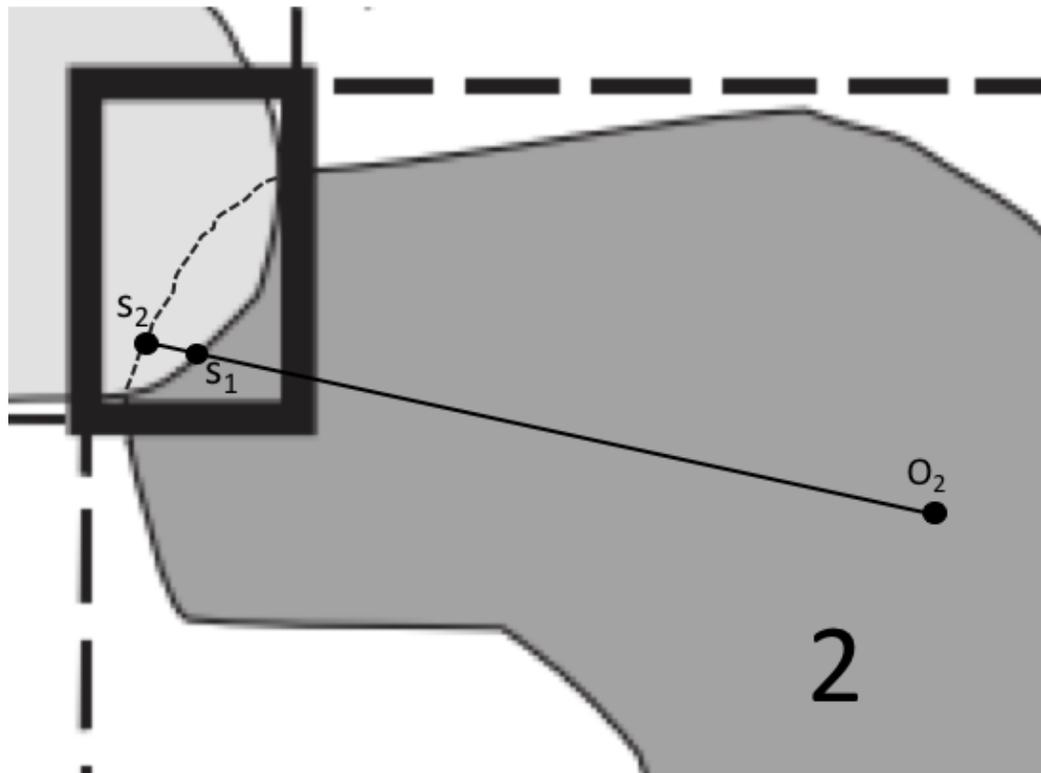
Fig. 1.6.   2D schematic showing the contact detection algorithm within EOB.

A quick check for overlap is first performed along the line connecting the center

of the two particles as shown in Fig. 2.5 to save computational cost. If there is no overlap

along the line of centers and an EOB has been detected, the surface of particle 1 is

scanned with a resolution of N_{box} within the EOB and checked if the surface points are

within the EOB. Though not very intuitive, it is possible that some part of the surface of

the particles within the angle range of the EOB is outside the box and those points do not

need to checked for overlap since it is not possible for those points to be overlapping the

other particle. From each surface point on particle 1 which is inside the EOB, an

imaginary line segment is drawn to the center of particle 2 (S_1O_2 in Fig. 1.6). Now the

line segment is extended to the surface of particle 2 (S_2O_2 in Fig. 1.6). If S_1O_2 is less than

S_2O_2 it can be concluded that the two particles overlap and vice versa. Clearly, this

method is purely a geometrical solution and does not rely on numerical iteration schemes, which are more straightforward and elegant.

Another significant recent development to the method for mathematically representing irregular shaped particles using spherical harmonic expansions is the addition of the uniform thickness shell to the particles (Garboczi and Bullard, 2013). This feature has several important applications such as the ability to model the interfacial transition zone (ITZ) found in concrete. The uniform thickness shell for a sphere is straightforward to imagine and to determine mathematically. For any given angle (θ_i, ϕ_i), the radius of the uniform thickness shell is just the sum of the radius vector of the original sphere $r(\theta_i, \phi_i)$ and the thickness vector $t(\theta_i, \phi_i)$, since the thickness vector is always parallel to the surface normal of the sphere. However, even for shapes such as ellipsoids, the radius vector may not be parallel to the surface normal vector. Hence, a numerical method to determine the extension to the radius vectors was developed (Garboczi and Bullard, 2013) such that the thickness vector normal to any surface point can be a prescribed value. The procedure to obtain the uniform thickness shell involves setting up a system of vector equations as shown in Eq. 2.1 and solving them numerically using the Newton-Raphson iteration method. Fig.2.10 illustrates the vectors that form the system of equations in Eq. 2.1. These set of vector equations are solved for a set of angles in the range [0-2π] chosen according to a 120-point Gaussian quadrature scheme (Scarborough, 1966). Though the angles could be chosen in a linear interval for solving these equations, using the Gaussian quadrature scheme reduces errors during numerical integration for calculating properties of the uniform thickness shell such as volume and surface area.

1.3 Research Objectives

The EOB method and the uniform thickness shell method are two recently developed algorithms (Garboczi and Bullard, 2013) for the spherical harmonic representation of irregular shapes. It is identified that the integration of the EOB method to detect contact can potentially improve the performance of generating the Anm model. The ability to add uniform thickness shells to particles in the Anm model can be used to control the minimum inter-particle distance between particles by not allowing the uniform thickness shells to overlap. If the purpose of the uniform thickness shell is to control the inter-particle distance, the final model should not contain the actual shells. However, allowing the uniform thickness shell to overlap other shells and particles increases the applicability of the Anm model. One implication of adding this capability to the Anm model is that the shell also becomes part of the output data and hence data visualization will be affected. It was identified that data parallelism can be introduced into the Anm model to allow the program to take advantage of the multi-threaded, multi-core processors available on most computers today and speed up the particle packing algorithm.

The objectives of this research can be summarized as follows:

(1) Integrate the EOB method into the Anm model and perform a quantitative study of the performance improvements.

(2) Integrate the ability to add uniform thickness shells to particles into the Anm model and study how it can affect the packing density of the model. In the process, also identify any drawbacks of this new algorithms.

(3) Identify performance bottlenecks in the code, implement shared-memory parallelism in the code and study the performance improvement gained by adding parallelism to the code.

(4) Introduce the ability to allow uniform thickness shells to overlap other particles and shells and explore data visualization techniques for overlapping shells using a 2D slicing method.

(5) Characterize the wall effect observed in the Anm model using the 2D slicing method and quantify it using the radial distribution function (RDF).

Objectives (1) to (3) have been previously accomplished and are published in a journal article and presented in Chapter 2. Objective (4) and (5) are presented in Chapter 3. The conclusions of this research are drawn in Chapter 4 along with some thoughts on the outlook of this research for the future.

1.4 References

Amirjanov, A. and Sobolev, K. (2008) 'Optimization of a Computer Simulation Model for Packing of Concrete Aggregates', *Particulate Science and Technology*, 26(4), pp. 380–395. doi: 10.1080/02726350802084580.

Bentz, D. P. (1997) 'Three-Dimensional Computer Simulation of Portland Cement Hydration and Microstructure Development', *Journal of the American Ceramic Society*. Wiley Online Library, 80(1), pp. 3–21.

Bentz, D. P., Garboczi, E. J., Bullard, J. W., Ferraris, C., Martys, N. and Stutzman, P. E. (2006) 'Virtual testing of cement and concrete', in *Significance of tests and properties of concrete and concrete-making materials*. ASTM International.

Bentz, D. P., Garboczi, E. J. and Snyder, K. A. (1999) *A hard core/soft shell microstructural model for studying percolation and transport in three-dimensional composite media*. US Department of Commerce, Technology Administration, National Institute of Standards and Technology.

Bullard, J. W. and Garboczi, E. J. (2006) 'A model investigation of the influence of particle shape on portland cement hydration', 36, pp. 1007–1015. doi: 10.1016/j.cemconres.2006.01.003.

Garboczi, E. J. (2002) 'Three-dimensional mathematical analysis of particle shape using X-ray tomography and spherical harmonics: Application to aggregates used in concrete', *Cement and Concrete Research*, 32(10), pp. 1621–1638. doi: 10.1016/S0008-8846(02)00836-0.

Garboczi, E. J. (2011) 'Three dimensional shape analysis of JSC-1A simulated lunar regolith particles', *Powder Technology*, 207(1–3), pp. 96–103. doi: 10.1016/j.powtec.2010.10.014.

Garboczi, E. J. and Bullard, J. W. (2013) 'Contact function, uniform-thickness shell volume, and convexity measure for 3D star-shaped random particles', *Powder Technology*. Elsevier B.V., 237, pp. 191–201. doi: 10.1016/j.powtec.2013.01.019.

Haecker, C.-J., Garboczi, E. J., Bullard, J. W., Bohn, R. B., Sun, Z., Shah, S. P. and Voigt, T. (2005) 'Modeling the linear elastic properties of Portland cement paste', *Cement and Concrete Research*. Elsevier, 35(10), pp. 1948–1960.

Jackson, M. D., Ciancio Rossetto, P., Kosso, C. K., Buonfiglio, M. and Marra, F. (2011) 'Building Materials of the Theatre of Marcellus, Rome*', *Archaeometry*, 53(4), pp. 728–742. doi: 10.1111/j.1475-4754.2010.00570.x.

Masoero, E., Del Gado, E., Pellenq, R. J.-M., Yip, S. and Ulm, F.-J. (2014) 'Nano-scale mechanics of colloidal C-S-H gels.', *Soft matter*, 10(3), pp. 491–9. doi: 10.1039/c3sm51815a.

Pellenq, R. J.-M., Kushima, A., Shahsavari, R., Van Vliet, K. J., Buehler, M. J., Yip, S. and Ulm, F.-J. (2009) 'A realistic molecular model of cement hydrates', *Proceedings of the National Academy of Sciences*. National Acad Sciences, 106(38), pp. 16102–16107.

Qian, Z. (2012) *Multiscale Modeling of Fracture Processes in Cementitious Materials*. Delft University of Technology, Netherlands.

Qian, Z., Garboczi, E. J., Ye, G. and Schlangen, E. (2014) 'Anm: a geometrical model for the composite structure of mortar and concrete using real-shape particles', *Materials and Structures*. Available at: http://link.springer.com/article/10.1617/s11527-014-0482-5 (Accessed: 24 January 2015).

Quiroga, P. and Fowler, D. (2004) 'The effects of aggregates characteristics on the performance of Portland cement concrete'. Available at: http://zanran_storage.s3.amazonaws.com/www.nssga.org/ContentPages/1117303 52.pdf (Accessed: 24 February 2014).

Scarborough, J. B. (1966) 'Numerical Mathematical Analysis Johns Hopkins U', *Press, Baltimore*, pp. 299–303.

Schaling, B. (2014) *The Boost C++ Libraries*. XML Press. Available at: https://books.google.com/books?id=Lkr7oQEACAAJ.

CHAPTER TWO: IMPROVED MODEL FOR THREE-DIMENSIONAL VIRTUAL

CONCRETE: ANM MODEL

This chapter is published by ASCE (American Society of Civil Engineers) in the

Journal of Computing in Civil Engineering and is referenced below:

Reference: Thomas, S., Lu, Y., & Garboczi, E. (2015). Improved Model for

Three-Dimensional Virtual Concrete: Anm Model. Journal of Computing in Civil

Engineering, 4015027. JOUR. https://doi.org/10.1061/(ASCE)CP.1943-5487.0000494

IMPROVED MODEL FOR THREE-DIMENSIONAL VIRTUAL CONCRETE:

ANM MODEL

Stephen Thomas[1]

Yang Lu, Ph.D., M.ASCE[2]

E. J. Garboczi[3]

Published in:

[1] *Graduate Research Assistant, Department of Materials Science & Engineering,*

Boise State University, Boise, ID 83725, USA

[2] *Assistant Professor, Department of Civil Engineering, Boise State University,*

Boise, ID 83725, USA

[3] *NIST Fellow, Applied Chemicals and Materials Division, National*

Institute of Standards and Technology, 325 Broadway MS 647, Boulder, CO

80305, USA

Abstract

Construction aggregate particles, fine or coarse, can be scanned by X-ray computed tomography and mathematically characterized using spherical harmonic series, and can then be used to simulate random parking of irregular aggregates to form a virtual mortar or concrete using the Anm model. Any other similar composite system of irregular (star-shaped) particles in a matrix can also be simulated. This paper integrates two new algorithms into the Anm model. The first new algorithm is the extent overlap box (EOB) method that detects interparticle contact, and the second is the capability of adding a uniform-thickness shell to each particle. Parameter analysis has shown that the EOB method leads to a more accurate detection of interparticle contact with a smaller computational cost than the previously used Newton-Raphson method. The uniform-thickness shell provides a customizable tool to control the minimum intersurface distance of particles during the parking process, as well as to simulate processes and microstructure that are dependent on the Euclidean distance from a particle surface. For mortar and concrete, the uniform-thickness shell can represent the observed interfacial transition zone (ITZ) structure. A parallel processing application programming interface (API) was integrated into the Anm model to accelerate the particle placement process by parallel optimization, which results in significant improvements in the packing efficiency on multicore processor systems. This significant speedup as well the improved contact function and new uniform-thickness shell algorithm greatly extend the range, size, and type of particle systems that can be studied.

2.1 Introduction

Concrete is primarily composed of coarse aggregates, fine aggregates (sand), and cement paste. Software packages like the Virtual Cement and Concrete Testing Laboratory (VCCTL) (Bentz et al. 2006; Bullard and Garboczi 2006) use computer-generated models to predict various properties of concrete. The accuracy of the models being used in the simulation plays an important role in predicting concrete behavior. Aggregate characteristics such as density and uniformity of aggregate packing and the corresponding particle size distribution (PSD) play a paramount role in strength and behavior of these concretes (Aïtcin 1998; Alexander and Mindess 2005; Neville 2011). Using realistic aggregate shapes instead of spheres (Amirjanov and Sobolev 2008) or ellipsoids can greatly improve the accuracy of such models in situations where aggregate shape is important, such as fresh concrete rheology, early-age mechanical properties, and fracture processes.

Aggregate shape and grading can significantly influence concrete workability (Koehler and Fowler 2007). Excessively flat and elongated aggregates typically have a lower packing density (PD) than more equiaxed aggregates, resulting in more paste being required to fill the voids between aggregates. There is a clear relationship between shape, texture, and grading of aggregates and the voids content of aggregates (Dewar 1999; De Larrard 1999). In fact, flaky, elongated, angular, and unfavorably graded particles lead to higher voids content than cubical, rounded, and well-graded particles. Further, these kinds of aggregates exhibit increased interparticle friction, resulting in reduced workability. Therefore, concrete mixtures with excessively flat and elongated aggregates often have higher water and cementitious materials requirements than concrete made with

normal aggregates. The proper selection of aggregates can minimize the water and cementitious materials contents needed to ensure adequate workability. Dense particle packing reduces paste consumption, thereby also providing significant cost savings (Kwan and Fung 2009; Kwan and Mora 2001). Models for predicting concrete compressive strength also base their validation on producing concrete mixtures of optimum packing density (Lecomte et al. 2005). An in-depth understanding of the packing of aggregates in concrete is therefore essential in optimizing the mix composition.

Typical models of concrete aggregates use spheres and ellipsoids as model aggregate particles, both because of the mathematical simplicity of defining these shapes and due to the lack of a sound method for determining the complete three-dimensional (3D) (real) shape of particles. Complete characterization of aggregate shape enables the use of real aggregate particles in 3D models. This is particularly important because it enables a controlled comparison of the different aggregate shape distributions. The characterization of aggregate shape is an important step towards the development of accurate particle packing models, which would otherwise not be possible. The evaluation of shape and texture is difficult and therefore the influence of aggregate shape and size has not been considered in ASTM or American Concrete Institute (ACI) concrete mixing standards. Some progress has been made regarding the problem of packing particles using regular shapes such as spheres (Sobolev and Amirjanov 2004) and ellipsoids (Xu et al. 2014a). Spheres with relatively smaller, equal-sized protruding hemispheres have also been used to model irregularly shaped dust particles (Goldasteh et al. 2012). Interparticle contact algorithms have been developed for polygons (Boon et al. 2012). With the

introduction of the method of using spherical harmonic series to represent and manipulate irregularly shaped particles (Garboczi 2002), it is possible to create more accurate models to simulate concrete microstructural behaviors and other complex particle systems.

The random shapes of real aggregate particles can be extracted using a combination of X-ray computed tomography (CT) (Garboczi 2002) or laser detection and ranging (LADAR) (Garboczi et al. 2006) and spherical harmonic analysis (Arfken 1970). This method can represent only irregular-shaped particles referred to as star-shaped particles (Max and Getzoff 1988). Irregular shapes can be characterized as star-shaped when any line segment connecting the particle's center of mass and a point on the surface is fully contained in the particle. Recently a material mesostructure model, entitled Anm, of mortar and concrete (Qian 2012; Qian et al. 2014) has been created using this idea of representing actual shapes of aggregate particles by spherical harmonic series. In this model, the irregularly shaped particles are randomly arranged in a cubic container where the packing algorithm is driven by PSD and PD. The PD is defined as the volume fraction of the aggregates within the simulation box. The particles are parked one at a time in decreasing order of size. Each particle is first assigned a random location within the container and checked for contact with any already parked particles. If an overlap is detected, a new location is attempted. If the particle could not be parked using a maximum number of locations, the particle shape is then randomly rotated for a predefined maximum number of attempts to find a location without overlap with other particles. If rotating the particle did not result in successful parking, it is rescaled within the current sieve size range. If the rescaling did not result in successful parking, a predefined number of alternate shapes are used to try and achieve successful parking. If

none of these attempts were successful in parking the particle from the current sieve, the next sieve is selected and this process is repeated. The Anm model can be used at several length scales. If the matrix is considered to be water, then the particles can be cement grains and the model represents fresh, fluid cement paste. If the matrix is cement paste, then the particles are sand grains and the model represents mortar, solid or fluid. If the matrix is considered to be mortar, then the particles are coarse aggregates and the model represents fluid or solid concrete.

When placing a particle, it is not very efficient, when there are more than a few particles, to search for overlap with all the previously parked particles in the entire container. Therefore, the container is divided into equal parts along the length, width, and height where each section is called a bin. Using the dimensions of each particle and its center point, it is possible to determine the bins it touches. Because the particles touching those bins are known, only that subset of particles needs to be checked for overlap instead of all the particles in the simulation box. This method of reducing the search extent is also known as spatial decomposition and is extensively used in collision detection (Jiménez and Segura 2008) of geometric object such as complex polyhedra. Some of the methods that rely on hierarchical data structures based on recursive subdivision of space are Quadtrees in two dimensions, Octrees in three dimensions (Ayala et al. 1985), AABB trees (Bergen 1997), and sphere trees (Bradshaw and O'Sullivan 2004).

The Anm model can use any arbitrary particle size distribution, described as a sieve analysis or sieve range. A certain volume fraction of the particles to be placed is located in each sieve size (e.g., 1 to 2 mm). Each sieve size is assigned a fraction of the total particle size distribution, such that the sum of volumes assigned to all the sieve

ranges add up to the total particle size distribution. In the Anm model, each sieve range volume must be occupied before placing particles from the next sieve range, starting from the largest sieve range.
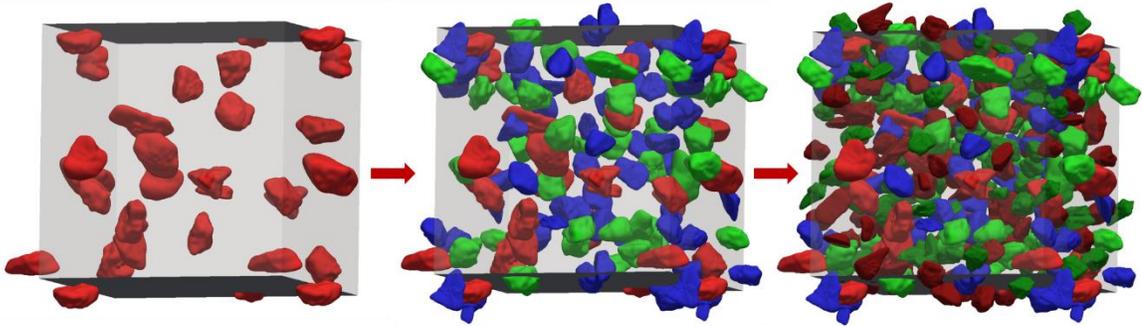
Fig. 2.1. **Placing star-shaped particles to model material mesostructure of mortar or concrete.**

Fig. 2.1 is the visualization of the progress of particle packing in the container. In this illustration, three sieve ranges are assigned in the following order: 8 to 10 mm, 6 to 8 mm, and 2 to 6 mm. The particle dimension used in the sieve range is the particle width (Erdoğan et al. 2007). The length of a particle is defined as the longest point-to-point distance in the particle, and the width is defined the same way except that it must be perpendicular to the length. Each sieve range is denoted by a parking group [parking is a synonym for placement (Cooper 1988), so there are three parking groups for this example, denoted big, middle, and small]. To achieve a higher packing density, the big-particle group containing particles of size 8 to 10 mm are picked up and placed as the first parking group. The packing algorithm will generate a certain number of random attempt locations to park particles one by one if there is no contact with current particles in the box. When the limit on the number of attempts is reached, a preset parameter, and still no location is found in which to park the current particle, particle placement from the big parking group is not possible any more. If all the particles have been placed, the

algorithm will go on to the next size group (middle size particles), which will be selected

and parked in the same manner. This procedure will be repeated until the final attempt

has been finished for the particles belonging to the smallest size parking group. The Anm

model allows placement of the particles according to either periodic or nonperiodic

boundary conditions. In nonperiodic boundary conditions, no particles are allowed to

extend beyond or even touch the sides of the unit cell, whereas when using periodic

boundary conditions particles that would extend beyond a unit cell boundary are allowed

and are checked against contact in the periodic direction. Ghost particles are created

whenever a particle is placed that has some portion extending beyond the unit cell

boundary (Qian 2012; Qian et al. 2014)

An algorithm that has been found to be useful with star-shaped particles is the

ability to coat a particle with a uniform-thickness shell (Garboczi and Bullard 2013). The

uniform-thickness shell can be used to simulate the interfacial transition zone (ITZ)

around aggregates in mortar and concrete. Results from Mondal et al. (2009) showed that

the ITZ is a relatively weak component of normal portland cement concrete and study of

networks formed by it can be critical for understanding failure. The uniform-thickness

shell can also be an effective tool for studying the wall effect (De Larrard 1999) found on

aggregate surfaces and for studying any process that depends on distance from a particle

surface. For a spherical particle of radius R and coating thickness t, this is an easy task—

just place another sphere concentric to the particle but with radius $R + t$. The space

between the two spheres has a uniform thickness t. For any other shape, making the

coating of uniform thickness at all points of the particle surface is not so easy. This

mathematical problem has been solved for star-shaped particles with a spherical

harmonic series representation. Such surface zones occur in many kinds of composite particle systems, so this algorithm, integrated into the Anm model, should have general utility. Henceforth, this uniform-thickness shell shall simply be referred to as shell in this paper. In addition, the ability to place shells around each particle means that the Euclidean distance from each particle's surface at every point of the surface can be known so that processes that are a function of distance from a particle surface can be more easily simulated.

In addition to the shell algorithm, two other important improvements to the Anm model, described and used in this paper, are establishing a new, faster, and more accurate particle contact algorithm, and adding a degree of parallelism into the Anm code so that it runs much faster than the original model (Qian 2012; Qian et al. 2014). Recently, the Anm model has been used to create high quality three-dimensional tetrahedral mesh (Lu and Garboczi 2014), demonstrating its applicability in microstructural corrosion modeling using finite-element analysis. The meshing method converts the 3D multiphase microstructure surface geometry created by the Anm model into a tetrahedral mesh without sacrificing the shape features.

The rest of this paper attempts to study the effects of using the new particle contact method and shell in the concrete mesostructure model. "Integration of New Search Algorithm" discusses integration of the new contact function into the Anm model. The method of adding a shell to the irregularly shaped particles is discussed in "Integration of the Uniform-Thickness Shell Algorithm into Anm." "Parallel Optimization of Anm Code for Faster Execution" briefly discusses the method to parallelize the algorithms, which greatly improve their efficiency. "Results and

Discussion" illustrates some results obtained with the improved Anm model.

"Conclusions and Future Research" concludes the discussions and projects the direction

of future research.

2.2 Integration of New Search Algorithm

Two spherical objects cannot overlap if the distance between their center points is

more than the sum of their radii. In the case of irregularly shaped particles, the method

for detecting contact is more complex. Previously, an analytical method, which solved

nonlinear equations using the Newton-Raphson (NR) iteration method, was employed to

detect contact between two spherical harmonic particles (Qian 2012; Qian et al. 2014).

The NR method was time-consuming due to its iterative approach and if the searching

tolerance was set too high, small overlaps could occur for some irregularly shape

particles even when the algorithm indicated that they were not overlapping.
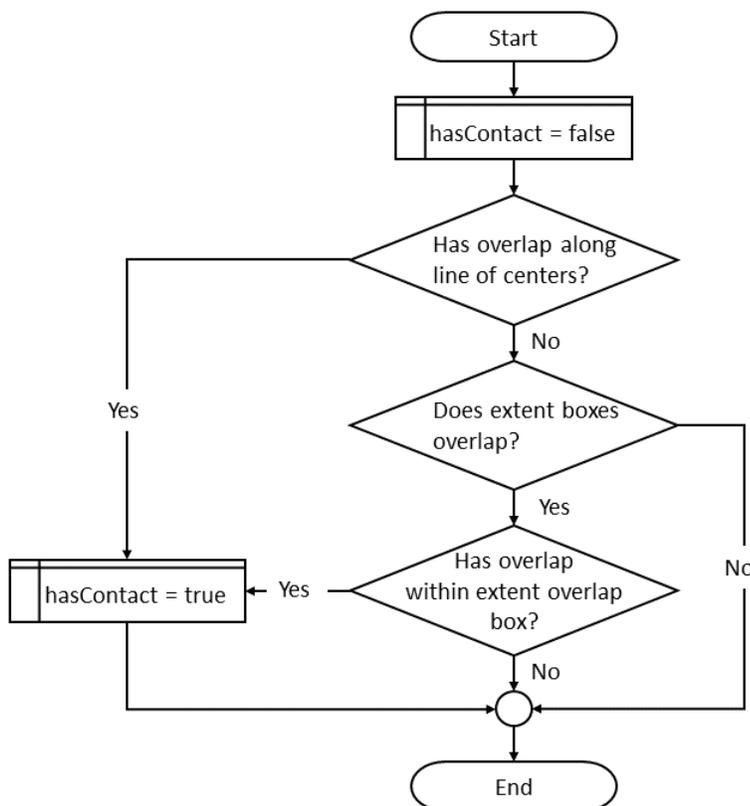
Fig. 2.2.   Three-step algorithm for searching contact.

The new method that has been added to the Anm model is called the extent

overlap box (EOB) search algorithm (Garboczi and Bullard 2013). A three-step process

as shown in Fig. 2.2 is followed in this algorithm with an increasing level of rigor to

search for a contact between the two particles in question. This is designed to increase the

throughput of the contact search process. The goal is to limit the most rigorous contact

search algorithm to particles with very minimal overlap. For example, if two particles

being considered have a large extent of overlap, overlap may be detected on the first or

second step, which is computationally cheap. However, for a situation such as in Fig. 2.3,

where there is only minimal contact between the particles, the contact is detected only in

the third step.
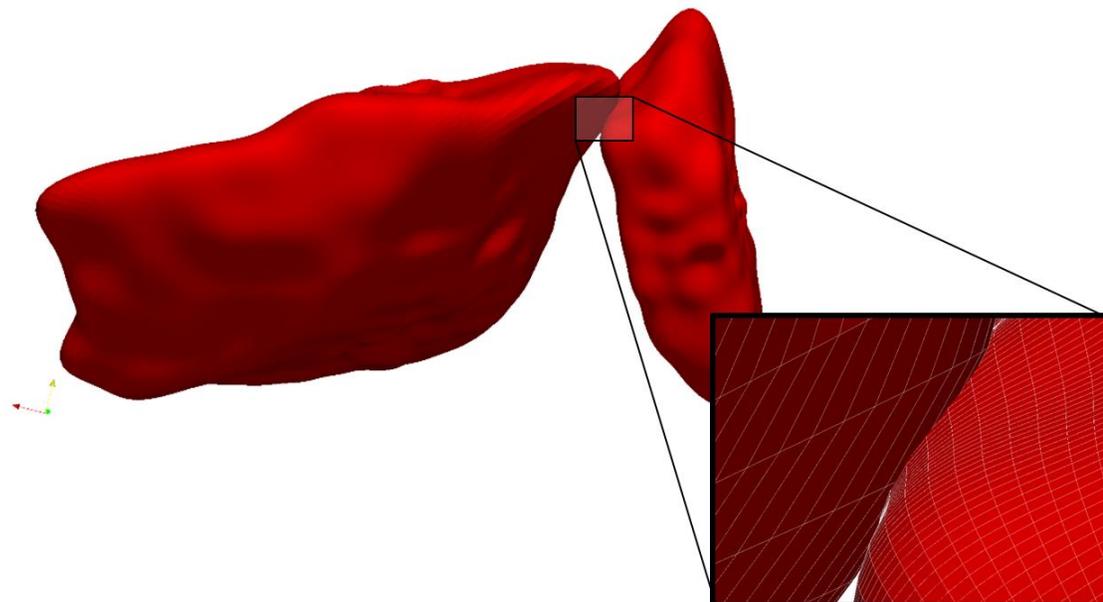
Fig. 2.3.   **Two particles with minimal overlap.**
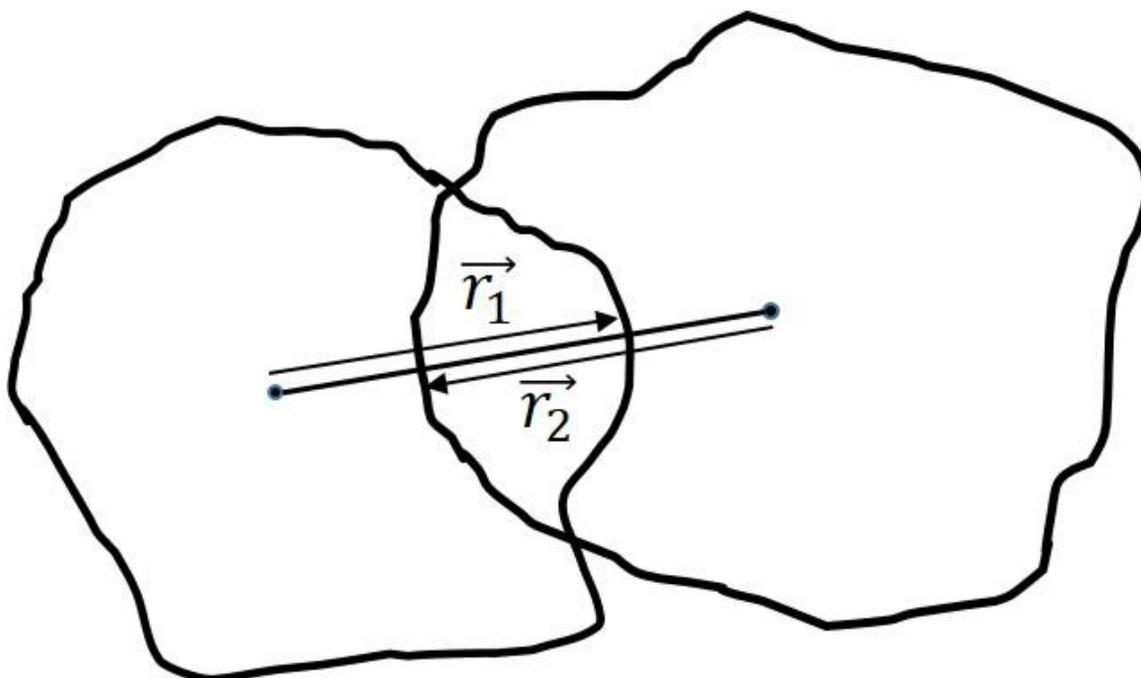
Fig. 2.4.   **Schematic representation of particles with overlap along line of centers shown in 2 dimensions. Here the sum of the individual radii ($\overrightarrow{r_1} + \overrightarrow{r_2}$) is greater than the length of the line of centers.**
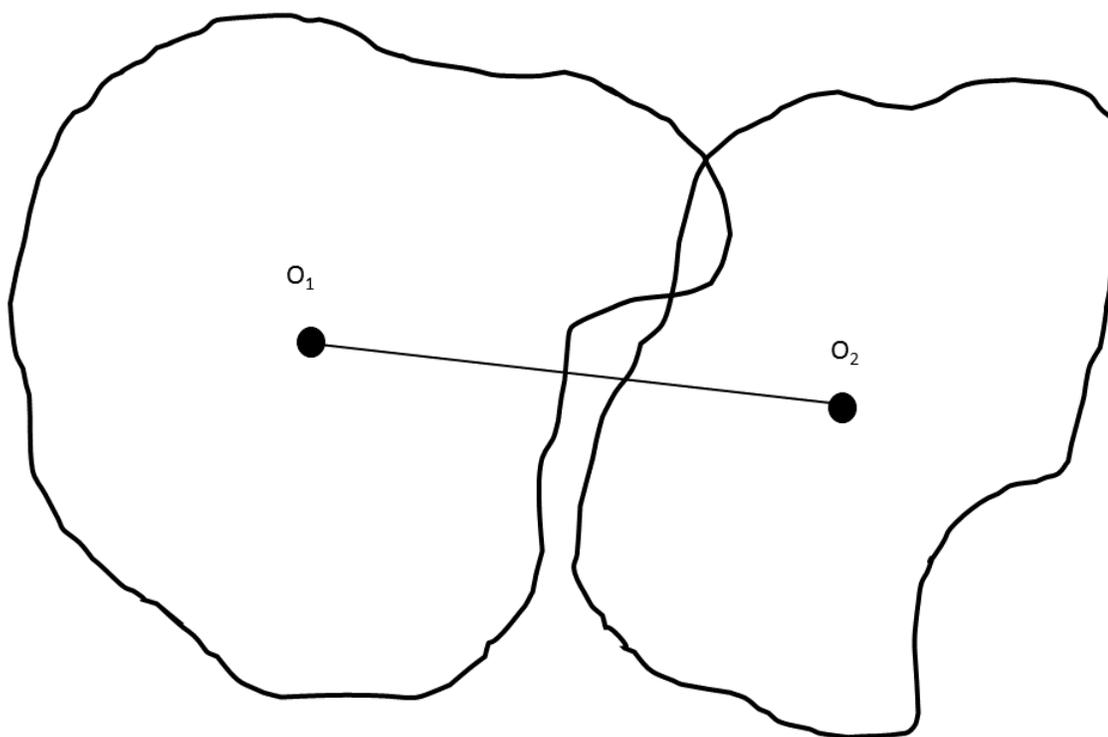
Fig. 2.5. **Schematic representation of two particles which do not overlap along the line of center points in 2 dimensions, but have a non-zero volume EOB.**

In the first step, the EOB algorithm attempts to search for an overlap along the line that connects the center point of the two particles. In order to do this, the radius of the particles along the direction given by the line joining the two center points is first calculated. If the sum of the radii is more than the length of this line, the particles are marked as overlapping, as is shown in Fig. 2.4. If they do not overlap along the line of centers, as schematically shown in Fig. 2.5, the extent box for both the particles are computed and an overlap in the extent boxes is identified if any exists.
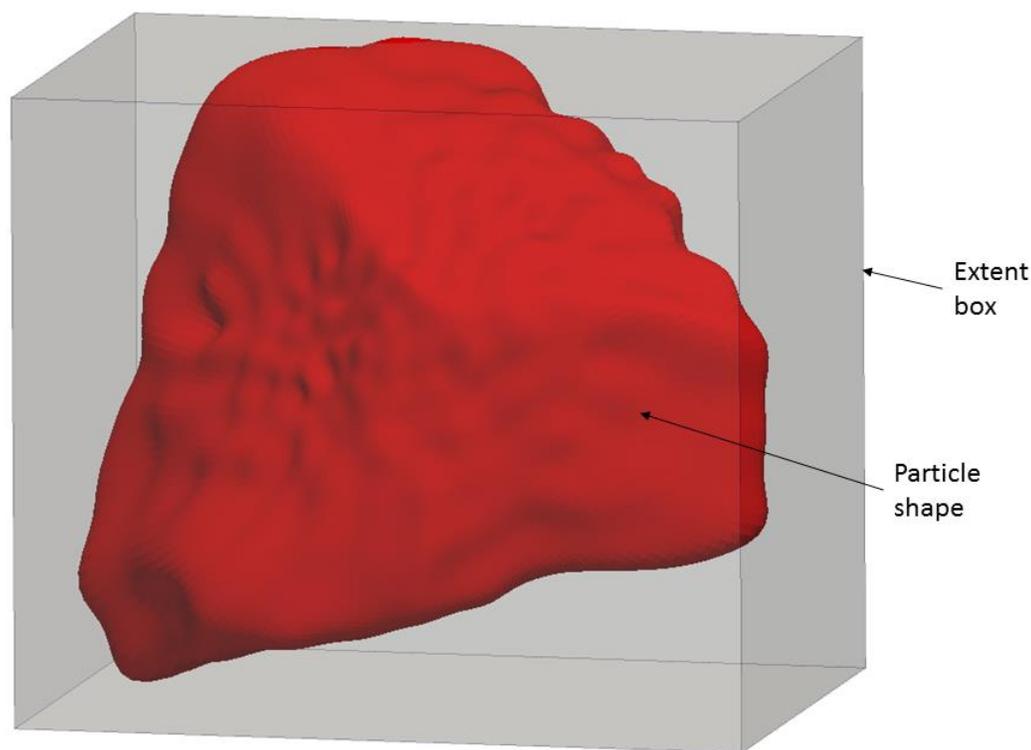
Fig. 2.6. **Extent box for an irregular shaped particle.**

The extent box is defined as a rectangular box surrounding the particle and touching it at only six points: the minimum and maximum values of x, y, and z on the particle's surface. Fig. 2.6 shows the visualization of the extent box for a particle. The accuracy of the size of the extent box depends on the number of intervals of θ and $\emptyset$ used to search for the six extrema. Here θ and $\emptyset$ represent the polar and azimuthal angles, respectively, in the spherical coordinate system and their values range from 0 to π and 0 to 2π, respectively. As the search intervals coarsen, there is a chance that certain parts of the particle go undetected and occur outside the extent box. This interval is controlled using a parameter called N_{ext}, which gives the number of angles to be used in both θ and $\emptyset$. In order to determine the optimum value for N_{ext}, the change in the volume and linear

dimension of the extent box (Vbox) was observed as the value of N_{ext} was increased (Garboczi and Bullard 2013).

If the extent boxes of two particles do not overlap each other, there is zero probability that the particles also overlap each other. But, if the two extent boxes do overlap, then the particles themselves can overlap only within the intersection of the extent boxes, which is itself a rectangular box called the EOB. The EOB is the only volume that needs be considered further to determine overlap or nonoverlap.
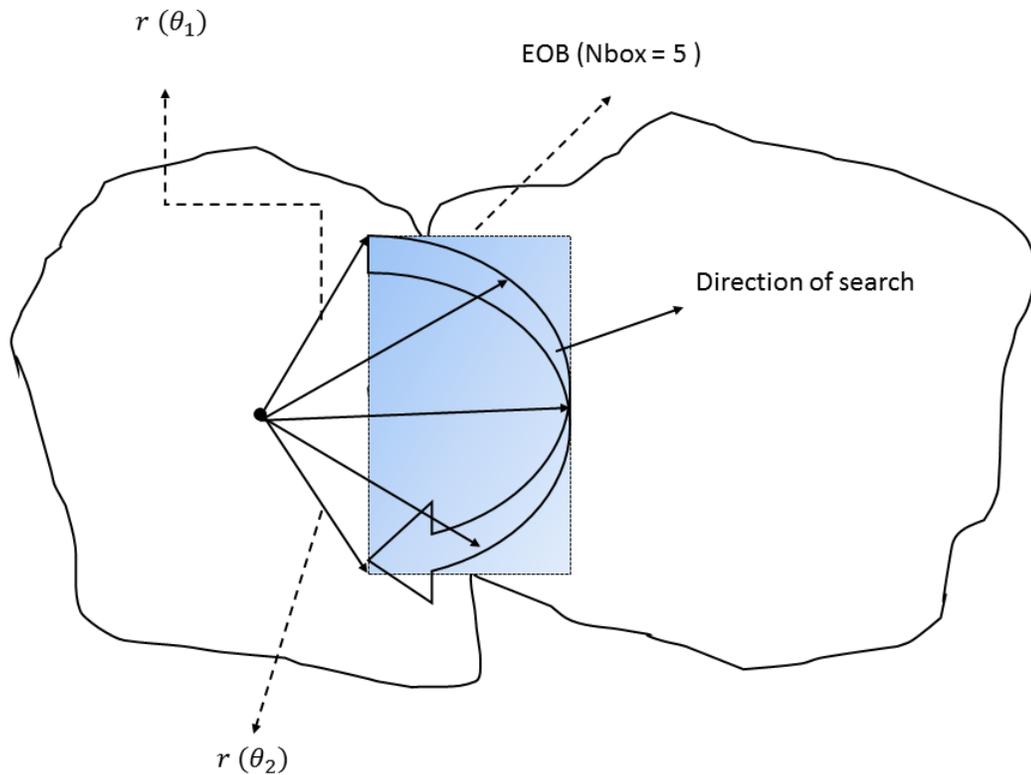
Fig. 2.7.   **Illustration of N_{box} value.**

$D_2 > D_1$, so $D_{overlap} = D_2$
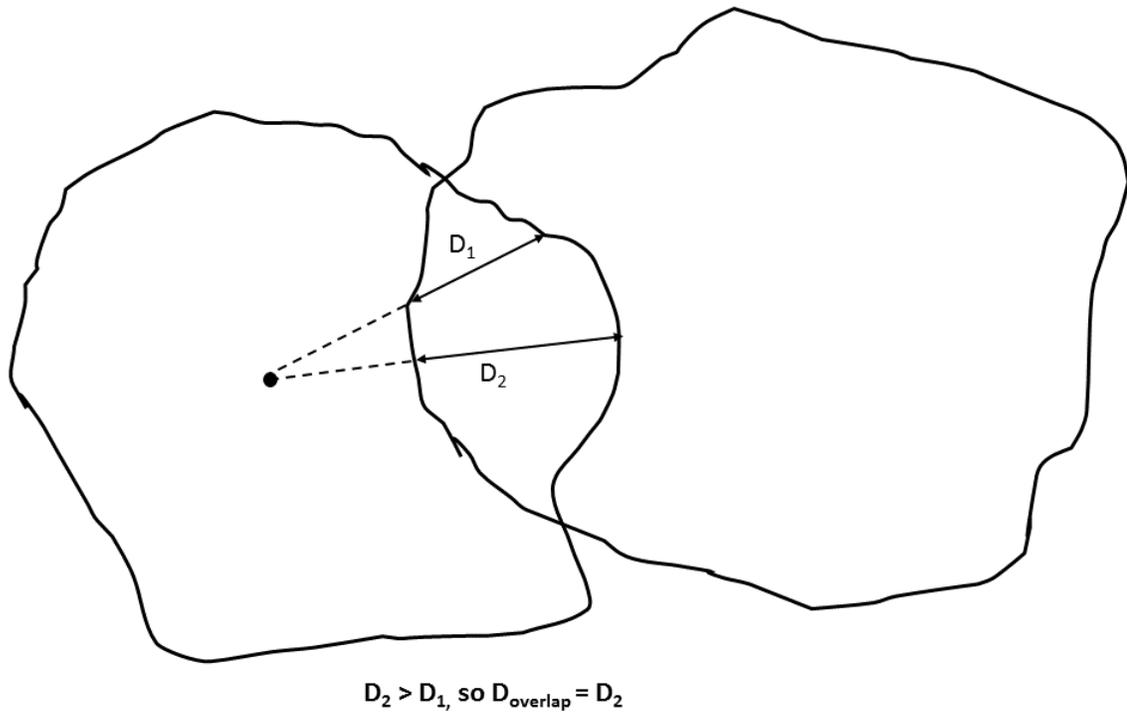
Fig. 2.8. **A two-dimensional illustration of the $D_{overlap}$ with respect to two overlapping irregular shaped particles.**

When two particles are found to have a nonzero volume EOB, the minimum and maximum values of θ and $\emptyset$ within the overlap box for each particle are determined. Then the surface points of the particle along those directions are scanned to check if any of those points are overlapped by the second particle. The accuracy and speed of this measurement is controlled using a parameter N_{box}, which is the number of surface points scanned along the range of each of these angles. Fig. 2.7 illustrates how N_{box} affects the contact search algorithm in a two-dimensional layout (considering only θ unlike the actual three-dimensional case with θ and $\emptyset$). Here because N_{box} is equal to 5 between angles θ_1 and θ_2, only five surface points are checked for contact. If the value of N_{box} is very small, the scanning is coarse and some overlaps may not be detected. As the value

of N_{box} increases, the scan becomes finer but computationally more expensive. So, the value of N_{box} determines the balance between the efficiency and the accuracy of this search. More quantitatively, the optimum value of N_{box} can be calculated by studying the maximum distance, denoted $D_{overlap}$, between the surfaces of the overlapped particles in any direction from the center of one of the particles. This distance is schematically represented in Fig. 2.8. For two particles with no overlap, the value of $D_{overlap}$ will be zero for any value of N_{box}. But for two overlapping particles, $D_{overlap}$ will have a nonzero value that is dependent on the value of N_{box}. Once the value of N_{box} is large enough, the value of $D_{overlap}$ does not change any more. A further increase in the value of N_{box} will not be useful because it will not increase the accuracy of the overlap determination.

More detailed analysis in "Results and Discussion" of the two barely overlapping particles shown in Fig. 2.3 will serve to describe the optimum values found for N_{ext} and N_{box}.

The EOB contact algorithm (Garboczi and Bullard 2013) is then faster than the Newton Raphson method (Qian, 2012;Qian *et al.*, 2014) because only the surface points on one particle that are also inside the EOB are checked for contact with the other particle. It is also more accurate than the Newton Raphson method because false negatives were not seen in an extensive series of visual checks.

2.3 Integration of the Uniform-Thickness Shell Algorithm into Anm

A uniform-thickness shell can be used to simulate the ITZ around aggregate particles in mortar and concrete. Crack development within normal portland cement concrete takes place inside the ITZs (Bentur et al. 2000; Ollivier et al. 1995). Results from Mondal et al. (2009) showed that the ITZ was found to be quite heterogeneous. A

higher concentration of large voids and cracks in the ITZ was observed. It was noted that

the connectivity of the weaker areas such as large voids and cracks along the interface

governs failure.
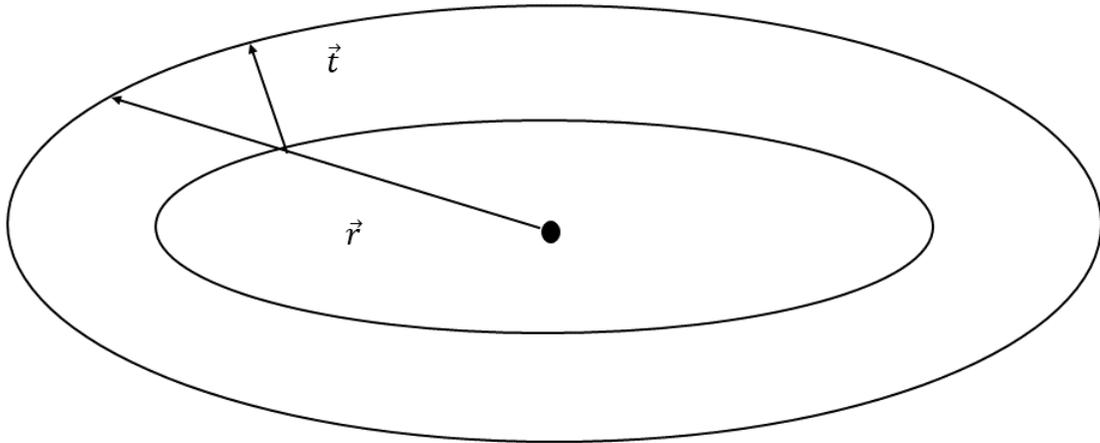
Fig. 2.9. **Adding a shell by increasing the length of the radius vector by different amounts at different original surface points.**

As was mentioned previously, a shell of thickness t added to a sphere with radius

R has a radius R' = R + t because the surface normal of a point on the sphere surface is

parallel to its radius vector. However, in the case of any shape other than a sphere, the

surface normal is in general not parallel to the radius vector from the center of mass.

From Fig. 2.9, it is obvious that the surface normal is not parallel to the radius vector in

an ellipse. In a star-shaped particle, a shell can be added by extending the radius vector

for each value of θ and $\emptyset$, such that the distance between the original surface and the new

shell measured along a surface normal vector originating from the same point on the

original surface is of length $|\vec{t}|$ (Garboczi and Bullard 2013). The length of the extended

radius vector is in principle different for every value of θ and $\emptyset$.
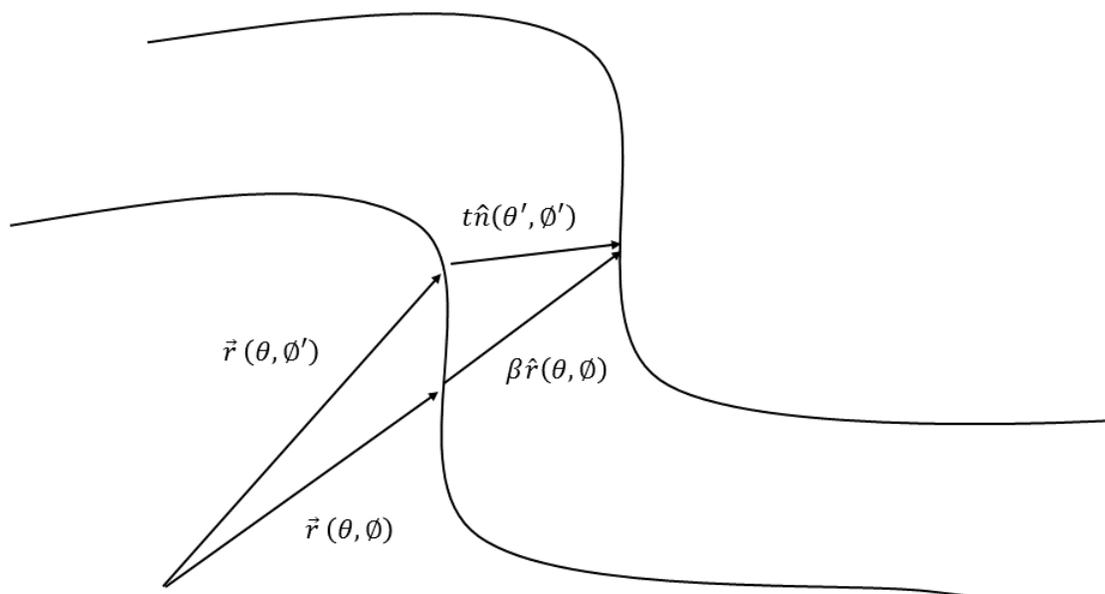
Fig. 2.10. Illustration of the vector equation with three unknowns $\boldsymbol{\beta}, \boldsymbol{\theta'}$ and $\boldsymbol{\emptyset'}$.
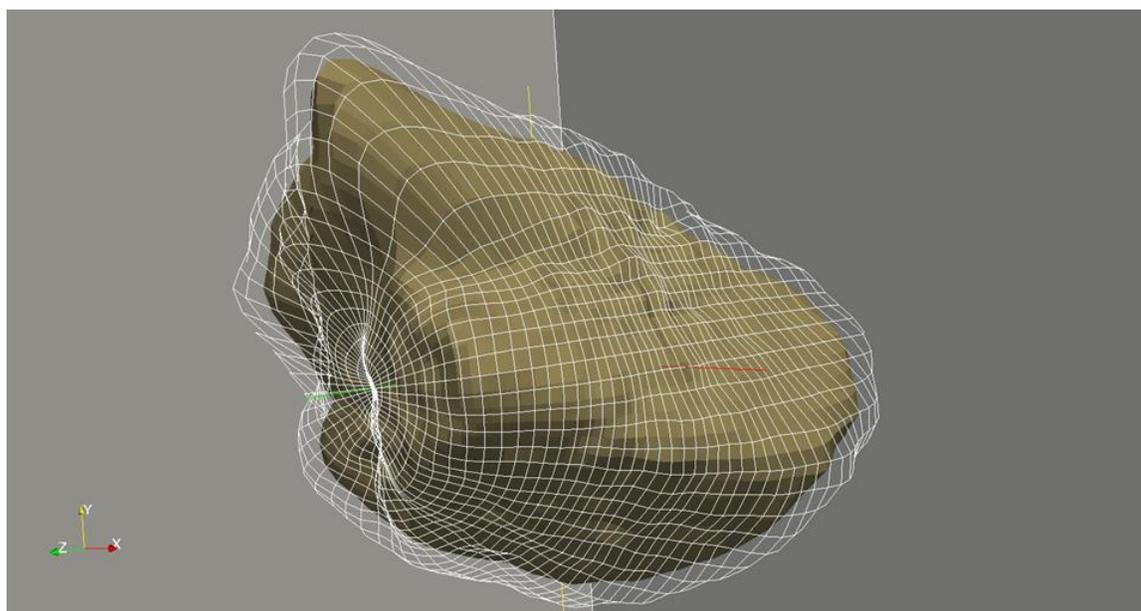
Fig. 2.11. Irregular particle with shell of thickness t = 0.2 % of particle length.

The length of the radius extension can be calculated by solving the vector Eq. (2.1) illustrated in Fig. 2.10, where t is the thickness and the unknowns are β, θ', and ∅'. The three equations and three unknowns give rise to a system of equations that can be solved using the Newton-Raphson method for each choice of θ and ∅ (Garboczi and Bullard 2013)

$$\vec{r}\,(\theta, \emptyset') + t\hat{n}(\theta', \emptyset') = \vec{r}(\theta, \emptyset) + \beta\hat{r}(\theta, \emptyset) \tag{2.1}$$

Fig. 2.11 shows a visualization of a shell around a single particle. The wired surface shows the shell, while the solid surface shows the original surface of the original irregularly shaped particle. Here particle length represents the largest surface-to-surface distance.

Once a shell is added to the particle, the particle along with its shell can be placed in three different ways. In the first option, no shells are allowed to overlap other shells or particles. In this situation, the minimum surface distance between any pair of particles is 2t. In the second option, the shells are allowed to overlap with other shells but not the other particles. In this situation, the minimum surface distance of two particles is t. In the third option, the shell can overlap with other particles, but still no contact is allowed between any two particles. In this situation, the minimum surface distance between two particles is zero. The second and third options are observed in particulate composites. The first option is implemented in the particle parking code in case it is needed. At a macroscale, these composite models are considered to consist of three phases: the star-shaped particles themselves, which follow a specific particle size distribution, the interfacial layer or shell, and the matrix. Each volume fraction can be readily computed.

The volume fraction of the interfacial layer or shell in other types of composite materials can be a significant contributor to macroscopic physical properties (Xu et al. 2014b).

The shell model, along with the original Anm model, has the potential to serve as a microstructural modeling tool in several areas of research that are difficult to do experimentally either due to the scale or due to the complexity of the materials. Two interesting studies that can benefit from this are the effects of ITZ on the electrical conductivity of mortar (Shane et al. 2000) and interfacial structures that have been found to have a significant effect on thermal conductivity of nanoparticle-fluid mixtures (Xie et al. 2005). More recently, the effect of ITZ on the diffusivity of chlorine in cementitious materials were also studied (Lu et al. 2012). In the chlorine diffusion research, the Anm model was employed to build a virtual mortar microstructure and a small surface crack was created on top of it to study the influence of crack on chlorine transport. The 3D multiphase microstructure meshing method (Lu and Garboczi 2014) was used to create 3D tetrahedral elements. The created 3D mesh was included in finite-element analysis for chlorine diffusion simulation.

2.4 Parallel Optimization of Anm Code for Faster Execution

The Anm code contains many time-consuming loops. Because the original program was designed for serial execution, irrespective of the number of processors present in the computer, only one of them was being utilized effectively. The CPU utilization was measured when the particle packing was executed on the test system running an Intel Core i7-4700HQ CPU (National Institute of Standards and Technology, Gaithersburg, Maryland) operating at 2.40 GHz (eight processors) with 12 GB of RAM.

The average CPU utilization of the test program was measured to be 12.4% ≈ 1=8. A typical pseudocode in such programs is shown in Fig. 2.12.

```
for (int i = start_value; i < end_value; i++)
{
    for ( int j = start_value; j < end_value; j++)
    {
        statement1;
    }
}
```

Fig. 2.12.   **Pseudo code for a typical serial code containing time consuming loops.**

```
parallel_for(start_value,end_value,[&](int i)
{
    for ( int j = start_value; j < end_value; j++)
    {
        statement1;
    }
});
```

Fig. 2.13.   **Pseudo code for time consuming loops after parallelization.**

The sequential code is not utilizing the maximum capacity of the multicore system. Parallel programming techniques can be used to allow the independent iterations to execute in parallel, utilizing the processors that are otherwise idle. For the purpose of this study, the authors chose to use the Microsoft Parallel Patterns Library (PPL) (Gebali 2011) to enable parallel execution of the code. The PPL library provides "*parallel_for*" constructs, which can be used to replace normal "*for*" loops to easily achieve parallel processing. After parallelization, the preceding pseudocode will take the form shown in Fig. 2.13.

Significant improvements were observed in the execution of the test program after incorporating the PPL. The test program now had an average CPU utilization of 87.9%. This improvement in performance is achieved by distributing tasks within the independent iterations in the pseudocode among many threads generated by the operating system. These threads have the ability to utilize the individual processors of the CPU concurrently. For instance, the algorithm for rotating particles in the Anm model concurrently manipulates surface points along the azimuthal angle (θ) in random order unlike a sequential code where the surface points will be manipulated sequentially along angles 0 to π. In this function, the Anm data representing a single particle shape are manipulated concurrently using multiple processors to achieve its rotation. Apart from the particle rotate function, similar parallelism has been implemented to the particle contact algorithm and uniform-thickness shell algorithm. Two types of parallelism can be achieved using the parallel libraries, namely, data parallelism and task parallelism. The method used in the Anm model as explained previously is an example of data parallelism and requires only minimal change from the sequential code. Task parallelism, on the other hand, is more effective in saving time but involves domain decomposition and distributive processing of task on different processors or computers (Subhlok et al. 1993). Therefore, introducing task parallelism requires more rigorous examination of the algorithm and redesign of the code, so is a good opportunity for further development.

2.5 Results and Discussion

2.5.1 Particle-Particle Contact Function

The EOB method is more efficient compared with the old NR method. The EOB method is faster than the NR method even without parallelization by approximately 19%.

The EOB method with parallelization (with eight processors) was found to be approximately 82% faster than the NR method (single processor). The simulation performed for this comparison packed particles from a coarse aggregate shape database into a cubic container of length 66 mm. The particle sizes were uniformly distributed from 7 to 11 mm. During the parking process, the authors recorded the time taken to check the overlap of 139 particle pairs for which the functions being compared were executed. A software timer was used to measure the time taken exclusively by the interparticle contact functions and the values were saved on a file by the program for analysis. The standard deviation of the execution time for the EOB method and NR method were 909 and 5,487 ms, respectively. The average execution times were 775 and 4,354 ms, respectively.
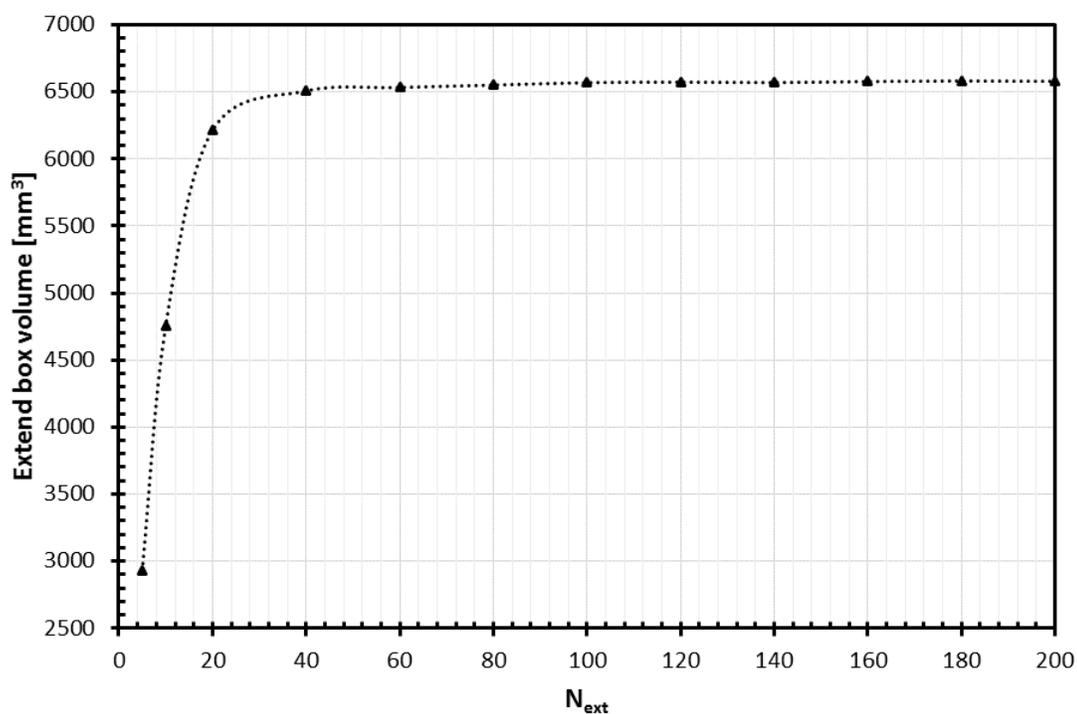
Fig. 2.14. **The effect of the value of N_{ext} on V_{box} for a single irregular shaped particle.**
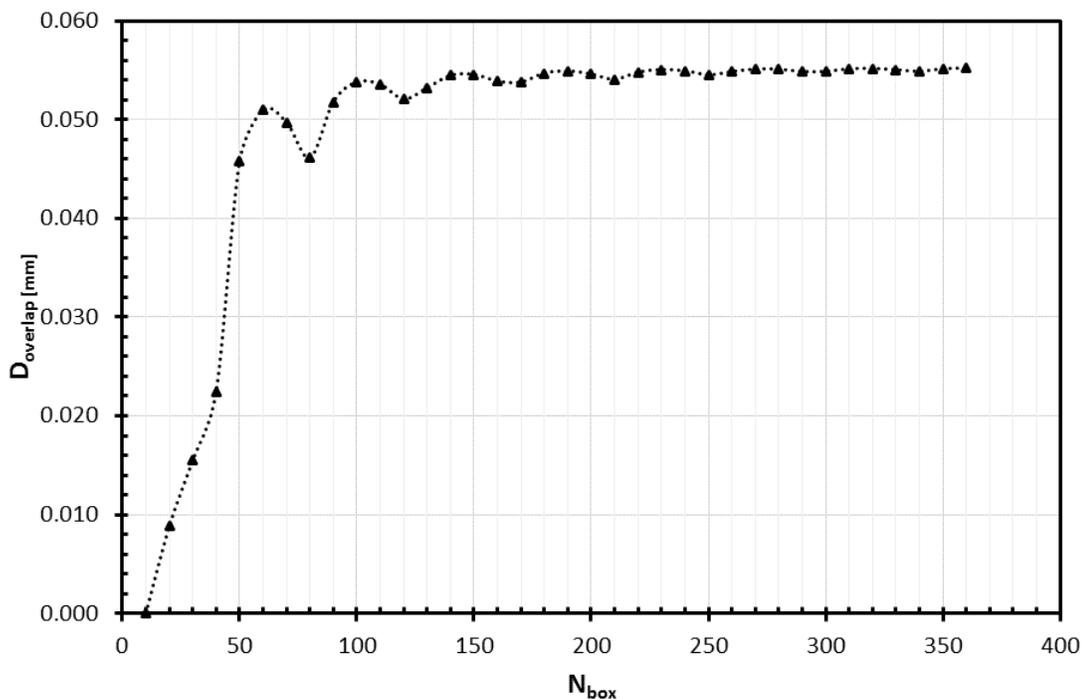
Fig. 2.15. The value of $D_{overlap}$ increases as the value of N_{box} increases for two particles with minimal overlap. The value of N_{ext} was fixed at 80 for this measurement.

The efficiency of the EOB method depends on two key parameters, N_{ext} and N_{box}. As explained in "Integration of New Search Algorithm," the optimum values for these parameters have been found by performing a parameter analysis. It can be seen in Fig. 2.14 that for values of $N_{ext} > 40$ there is very little change in the extent box volume. For values of $N_{ext} < 40$, the extent box volume still varies significantly with the value of N_{ext}. It can also be seen in Fig. 2.15 that beyond $N_{box} \approx 90$, there is very little variation in the value of $D_{overlap}$ so that increasing the value N_{box} beyond this point should not increase the accuracy of the overlap calculation. Thus, it is reasonable to use $N_{ext} = 40$ and $N_{box} = 90$ for the given sample particle database. With the optimum values of N_{ext} and N_{box} used, the EOB method will maintain a balance between efficiency and contact detection accuracy. Even though these optimal values were determined for only one aggregate, the

structure of the spherical harmonic representation means that these values do not vary much across an aggregate type.

2.5.2 Uniform-Thickness Shell

The shell algorithm in "Integration of the Uniform-Thickness Shell Algorithm in Anm" considers only small values of shell thickness, t, so that there is no shell-shell or shell-particle overlap between the shell and the particle (Garboczi and Bullard 2013) when computing the shell for each particle. These kinds of overlaps introduce numerical instabilities. The authors have found that the thickness of a single shell, t, should be limited to 0.1% of the particle length to avoid this condition in the specific case of the several kinds of coarse aggregates studied so far. Parameter analysis has been performed with shell thickness from 0.1 to 2% of particle length. If a thick shell is desired, it is also more numerically stable to sequentially add several thin shells rather than using a single thick shell.

An interesting question discussed earlier (Garboczi and Bullard 2013) was if there was any difference in creating a single shell of thickness 5t or five shells of thickness t. Shells were added to a particle, first as a single shell of 0.1% thickness, then 10 shells with 0.01% thickness each, and finally 100 shells with 0.001% thickness relative to the particle length. The authors observed that the volume of the new particle remains the same. The overall time taken to create the uniform thickness increased approximately linearly because a similar shell generation algorithm is repeated more times for the larger number of shells.

Another interesting question that can be addressed is how the particle density of the Anm model is affected by different values of the uniform shell thickness used during

the parking when the shells are not allowed to overlap. The authors simulated a cubic container with an edge length of 66 mm and parked particles from a coarse aggregate shape database with sizes ranging from 7 to 11 mm. The gradation was defined by four sieves: Sieve 1 (particle width ranging from 10 to 11 mm), Sieve 2 (9 to 10 mm), Sieve 3 (8 to 9 mm), and Sieve 4 (7 to 8 mm). The suggested fraction (volume fraction of total volume) of particles to be parked from each sieve is 0.25 and the suggested total PD of the simulation box is 0.25. The maximum number of random locations attempted with each sieve range is set to 2,000, whereas the number of random shape, orientation, and size attempts are all set to 1. The shell size was gradually increased from 0 to 2% of the particle length and its effect on the resulting simulation box was observed.

Table 2.1 **Particle size distribution and achieved volume fraction by particles from individual sieves**

Shell thickness (%)	Sieve 1 (10-11mm)	Sieve 2 (9-10 mm)	Sieve 3 (8-9 mm)	Sieve 4 (7-8 mm)	Total PD
0	0.2569	0.2540	0.2519	0.2524	0.2632
0.2	0.2569	0.2522	0.2503	0.2504	0.2619
0.4	0.2569	0.2523	0.2511	0.2514	0.2623
0.6	0.2575	0.2538	0.2530	0.2503	0.2631
0.8	0.2575	0.2538	0.2523	0.2416	0.2607
1	0.2505	0.2532	0.2524	0.2136	0.2514
1.2	0.2503	0.2507	0.2526	0.2473	0.2595
1.4	0.2503	0.2513	0.2525	0.1758	0.2411
1.6	0.2503	0.2521	0.2521	0.2081	0.2496
1.8	0.2501	0.2511	0.2511	0.2122	0.2501
2	0.2501	0.2520	0.2514	0.1952	0.2460

Table 2.1 describes the actual particle size distribution and individual PD achieved by each sieve. Generally, the PD is expected to reduce as the shell thickness increases because the particles with shell have a larger volume compared with particles without the shell. Due to this reason, the volume of particles that can be accommodated in the fixed-volume box is reduced. This lack of available space is first experienced by the particles parked last. It can be seen that Sieve 4, the smallest sieve, experiences a decreasing trend in PD. It is reasonable to assume that if the shell thickness is further increased this effect will be noticed on Sieve 3, Sieve 2, and so forth.

Table 2.2.   Number of particles per sieve with respect to the change in shell thickness of the individual particles.

Shell thickness (%)	Sieve 1 (10-11mm)	Sieve 2 (9-10 mm)	Sieve 3 (8-9 mm)	Sieve 4 (7-8 mm)	Total
0	50	67	89	126	332
0.2	50	66	89	126	331
0.4	50	66	91	125	332
0.6	50	66	88	127	331
0.8	50	66	89	124	329
1	49	66	91	110	316
1.2	49	65	89	125	328
1.4	49	65	90	91	295
1.6	49	65	89	107	310
1.8	49	66	90	110	315
2	49	66	90	100	305

In this simulation, there are other factors influencing the packing of the particles. The random packing does not result in a reliable dense packing where all the particles are almost touching their neighbors. Without the shell, many particles are already parked separately by a distance larger than the thin shell. Therefore, only a fraction of the particles that are almost touching their neighbors is influenced by the shell and contribute to a reducing PD. Sometimes, such particles that fail to park in a particular location due to the presence of the shell may favorably alter the random packing sequence, resulting in a slight increase in the number of particles parked. This effect is noticed in Table 2.1, in

Sieve 4, for shell thickness of 1.2 and 1.6%. Table 2.2 shows the actual number of particles parked from each sieve.
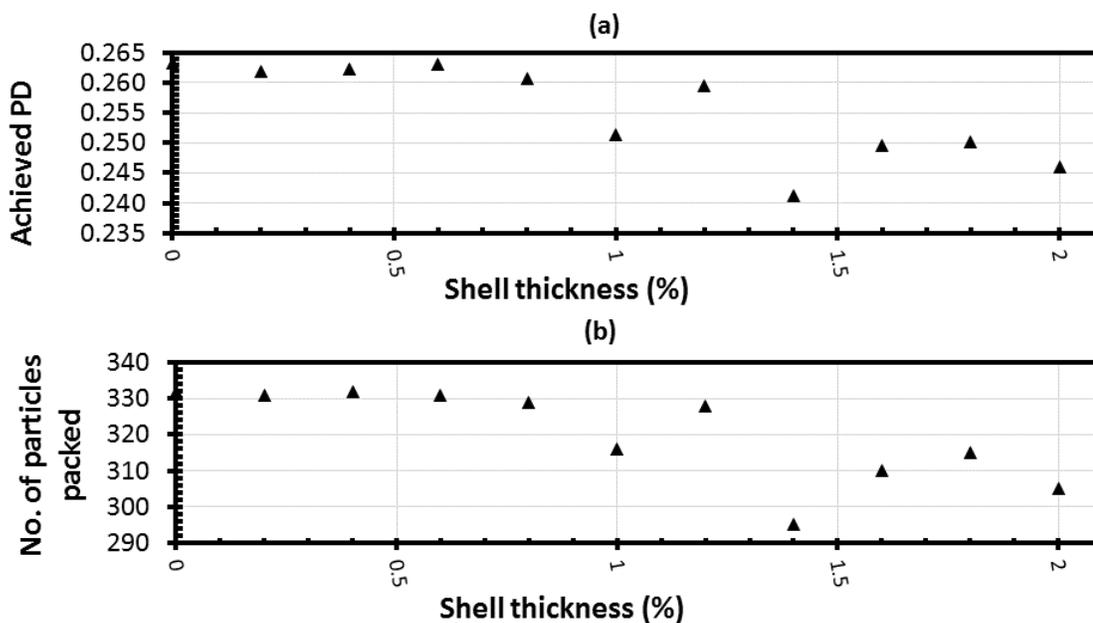
Fig. 2.16.   **Illustration of the (a) decreasing trend in PD and (b) number of particles packed with the increase in shell thickness.**
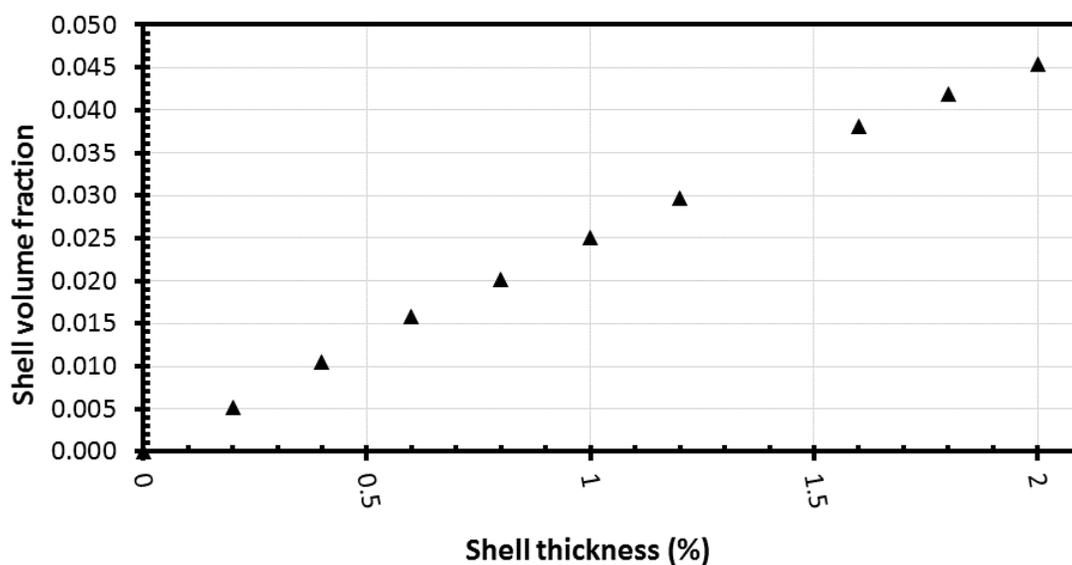
Fig. 2.17.   **Illustration of the linear increase in shell volume fraction with the increase in shell thickness.**

Fig. 2.16(a) illustrates the trend of PD and Fig. 2.16(b) illustrates the number of particles parked. Fig. 2.17 illustrates the trend in the total shell volume fraction for this

particular study. The total shell volume fraction increases. The overall packing density has a close correlation with the total number of particles packed. It is also observed that the volume fraction of the shell increased by ∼4.5%, the achieved PD dropped by ∼6.5%, and the total number of particles dropped ∼8% as the shell thickness is increased from 0 to 2% of the individual particle length. Overall, the addition of shell will affect the PD. With the increase of the shell thickness, the PD will be reduced. The thicker the shell, the less particles can be packed.

2.5.3 Effect of Random Locations on Packing Density and Particle Size Distribution

In the Anm model, there are four internal particle placement parameters: the number of random locations attempted, the number of random orientations attempted, the number of particle widths in a given sieve range attempted, and the number of random shapes.

In the Anm model, a particle with a specific shape, orientation, and width is selected and an attempt is made to place it at a random location within the container. If this attempt fails because of an overlap with another parked particle, a different random location is chosen within the container and an attempt is made to place it again. However, this cannot be done indefinitely. So, a maximum number of random locations are attempted before trying to use another random particle shape, width, or orientation. These are parameters for the maximum number of shapes, widths, and orientations allowed, thus it can be said that there are four sources of randomness in this algorithm. In principal, all four will contribute to the particle placement efficiency and the value of PD that is achievable. However, the authors identified the random location parameter as the most effective parameter for increasing PD based on their numerical particle packing

experience. Additionally, its low computational cost allows the use of many random trials

with- out unreasonably increasing the execution time. In the following study, coarse

aggregate shapes ranging from 4.75 to 11 mm were packed in decreasing order of size in

a cubic container having an edge length of 66 mm. The intended value of the PD was

0.355. Similar to the study that resulted in Table 2.1 and 2.2, the random locations

parameter was varied while keeping the other random parameters fixed.

Table 2.3.   Changes in PD and PSD of the Anm model as the number of random locations attempted for each particle is increased.

No. of random locations	No. of particles packed	Achieved PD	Sieve 1 10 mm to 11 mm (0.18)	Sieve 2 9 mm to 10 mm (0.18)	Sieve 3 8 mm to 9 mm (0.18)	Sieve 4 7 mm to 8 mm (0.18)	Sieve 5 6 mm to7mm (0.18)	Sieve 6 4.75 mm to 6 mm (0.10)
30	380	0.207	0.183	0.174	0.054	0.064	0.018	0.087
60	392	0.220	0.183	0.129	0.119	0.082	0.040	0.065
90	354	0.214	0.183	0.129	0.182	0.026	0.018	0.063
120	340	0.230	0.183	0.181	0.134	0.050	0.084	0.014
140	348	0.240	0.183	0.181	0.180	0.028	0.092	0.010
285	416	0.249	0.183	0.181	0.183	0.066	0.018	0.069
450	426	0.255	0.183	0.181	0.183	0.066	0.042	0.063
975	450	0.281	0.183	0.181	0.183	0.123	0.098	0.023
1500	510	0.295	0.183	0.181	0.183	0.174	0.042	0.068

In Table 2.3, contrary to intuition, the PD is reduced when the locations attempts

were increased from 60 to 90. This phenomenon can be understood by analyzing the

individual PD of Sieve 3. While attempting to pack the particles with 90 locations, Sieve

1 and 2 particles packed exactly the same amount as that of 60 locations. But Sieve 3

particles benefited from the increased number of attempted random locations and packed

better. These particles filled up a significant amount of empty space, leaving the

subsequent sieve particles less available space to pack. Upon careful examination of

Table 3, it is noticed that this phenomenon is repeated further down in smaller sieves as

the number of random locations are increased to 140, 450, and 1,500. However, the overall PD does not decrease for these cases, as was seen when going from 60 to 90 placement attempts, due to the smaller particle sizes (Sieves 4, 5, and 6) affected. The periodic packing method seems to generate a slightly denser packing compared with the nonperiodic packing method, which is expected because more efficient use would be made of regions near the edge of the cell when employing periodic boundary conditions. As the random location attempts were increased, it was observed that the larger particles, which are parked first, began to pack more densely and achieve the suggested volume fraction for their sieve range. The smaller particles, which are parked last, may require a larger number of random location attempts to reach their suggested volume fraction for each sieve due to higher PD of the particles from the prior sieves. Currently, all the sieves are assigned the same number of random location attempts and this value is usually a large value suitable for the last sieve being used. This raises a reasonable question about the possibility of using a different number of random locations for different sieves such that the last sieve is entitled to many more attempts than the first sieve. However, the program stops parking particles from a sieve when either the maximum number of random trials have been attempted or the suggested volume fraction has been parked. Due to this dual criterion for sieves, the sieves used in the beginning do not encounter the former condition if the suggested volume fraction of that sieve and the overall PD is reasonable. In contrast, the last sieve irrespective of the size of the particles in it will require a relatively large number of attempts due to the fact that the simulation box is already crowded with particles.

2.5.4 Performance Comparison

This section compares the performance of serial processing to the parallel computing achieved using the PPL. The most time-consuming loops were identified in the existing program and were upgraded with the PPL. Figs. 2.18 and 2.19 show the comparative time (in milliseconds) taken to execute two different functions in serial and parallel. Fig. 2.18 indicates the comparison of time taken to rotate a particle using serial and parallel execution of the algorithm. The parallel version has accelerated the particle manipulation operations significantly.
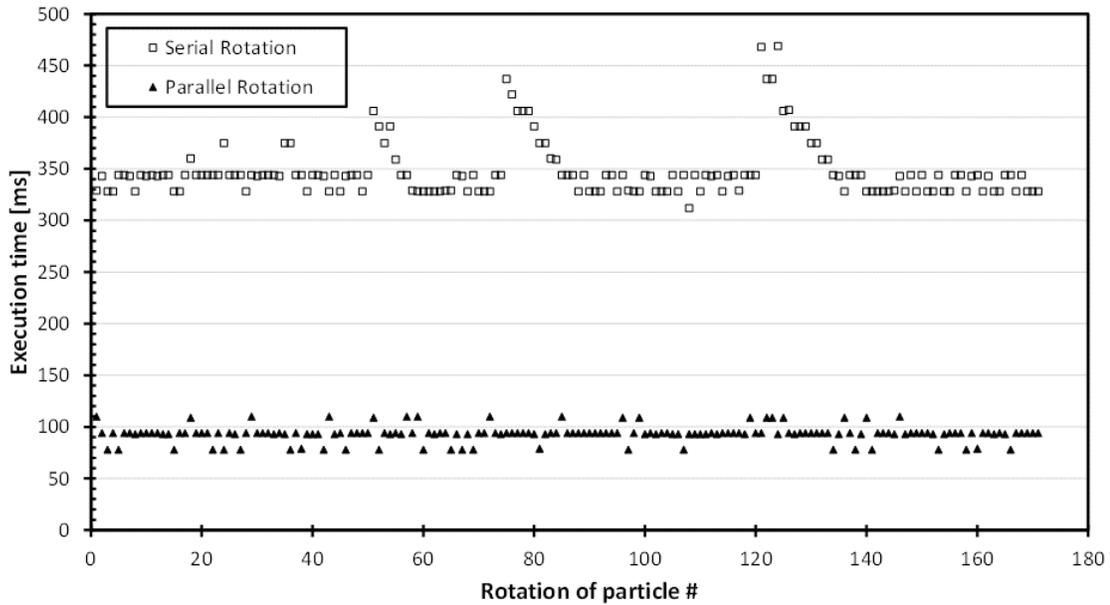
Fig. 2.18. **Comparison of time taken to rotate a particle using serial and parallel execution (8 processors) of the algorithm.**
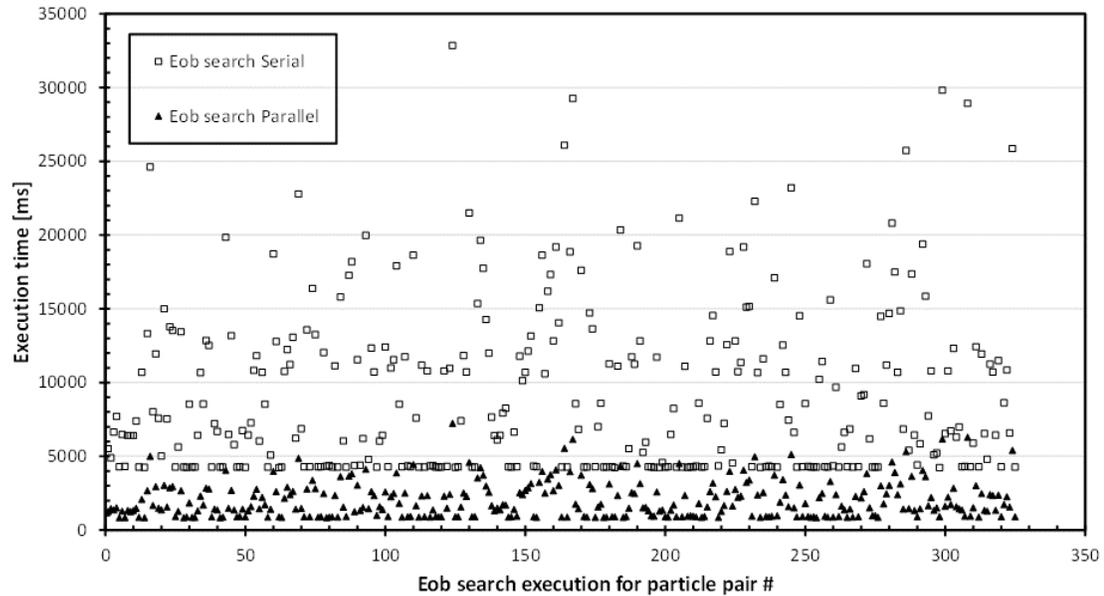
Fig. 2.19.   Comparison of the EOB contact searching algorithm using serial and parallel execution (8 processors).

Fig. 2.19 shows comparison of the EOB contact searching algorithm using serial and parallel execution. The large variations of serial run time shown in Fig. 2.19 can be attributed to the fact that as the extent of the overlap between the two particles in question decreases, the overlap detection requires more computation time. The parallel contact function reduces the computational load to some extent by randomly scanning points on the extent overlap box. This random scanning process has a higher probability of finding an overlap faster when compared with the sequential and ordered scan in the serial code. Apart from this advantage, the parallel code utilizes multiple processors available to process the data, thereby reducing computational load.

To analyze the advantage of using any parallel library over asequential program, two parameters are used, speedup and efficiency (Rauber 2010). While speedup provides a measure of benefit from using parallel libraries, efficiency gives an idea of the extent to

which a program is designed to be executed in parallel. The speedup parameter is defined

by Eq. (2.2)

$$S_p(n) = \frac{T^*(n)}{T_p(n)} \tag{2.2}$$

where $S_p(n)$ = speedup; $T^*(n)$ = execution time of the best sequential

implementation to solve the same problem of size n; and $T_p(n)$ = execution time of the

parallel execution using p processors. Linear speedup is achieved when

$$S_p(n) = p. \tag{2.3}$$

Efficiency is given by

$$E_p(n) = \frac{S_p(n)}{p}. \tag{2.4}$$

Ideal speedup $S_p(n) = p$ corresponds to an efficiency of

$$E_p(n) = 1. \tag{2.5}$$

The number of available cores for the test is 8

Particle placement attempts
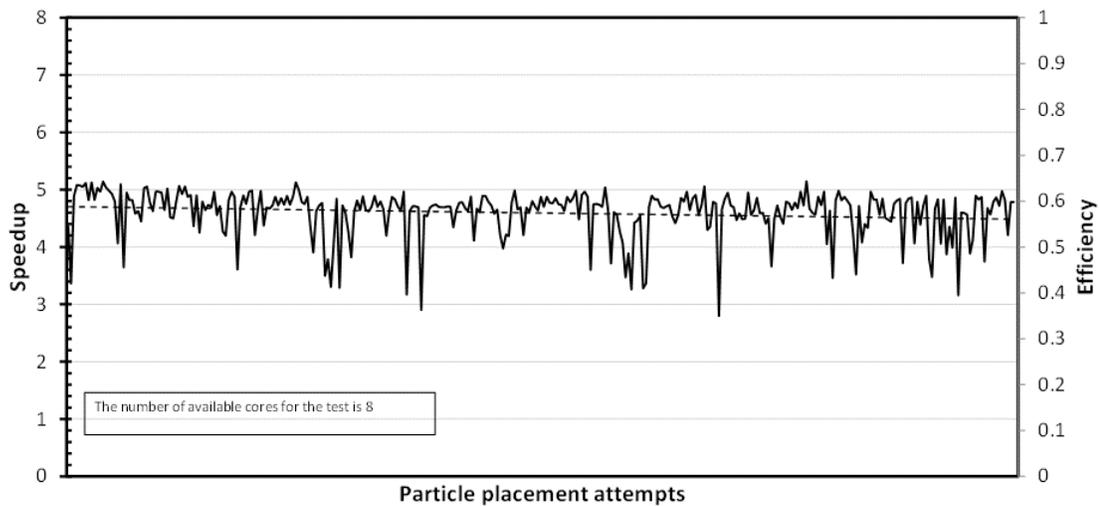
Fig. 2.20.   Efficiency of contact searching algorithm where the number of participating processors p=8.

Using the parallel efficiency concept, the efficiency of the contact searching

algorithm was investigated, where the number of participating processors (p) was 8. The

results shown in Fig. 2.20 indicate that a speedup of around 5 and an efficiency of close to 0.6 was achieved with the current parallel mechanism. This is a substantial improvement in performance compared with the sequential execution with a minimal amount of change in the code. The improvement in performance is not linear because only data parallelization has been implemented in the current version. Examples for data parallelism include the individual particle rotation function and two-particle contact function using the EOB method. However, there are other parts of the code, such as the particle parking function that parks one particle at a time sequentially. Parallelizing this function using task parallelism techniques such as message passing interface (MPI) is expected to produce a nearly linear performance improvement.

2.6 Conclusions and Future Research

Particle size distribution effects have been studied and standardized in ASTM standards (Lamond and Pielert 2006), but particle shape effects have not been extensively studied because of their complexity. The Anm model provides an effective method to simulate the proportioning of the aggregates considering real particle shape effects in concrete. The microstructure of mortar and concrete, or indeed any such composite material that can be modelled by star-shaped particles embedded in a matrix, can be simulated using the Anm model, which has been greatly improved and augmented. The following conclusions are made based on the results presented here:

- The EOB method is more efficient and accurate for the detection of interparticle contact when compared with the NR method used by the first version of the Anm model.

- The uniform-thickness shell provides a customizable tool to control the minimum intersurface distance of particles during the parking process. The shell also provides a

valuable method to simulate the highly heterogeneous properties of an interfacial transition zone around the particles. The two main factors that determine the effect of the nonoverlapping shells on achieved PD is the shell thickness t and the number of attempts to place the particles at random locations.

- Using the parallel processing application programming interface (API) framework, a speedup of approximately 5 and an efficiency close to 0.6 was achieved with the current parallel mechanism. This is a substantial improvement in performance compared with sequential execution using only a minimal amount of code change.

Future research will focus on more efficient parking methods that need to be devised to create more realistic models of the concrete microstructure, especially if size scales, like those between fine and coarse aggregate in concrete, are to be mixed. Task parallelization in addition to the present data parallelization will be studied. One of the focus areas will be to improve the parking density so that more realistically dense systems can be generated and studied. Applications will be generated as well as continually improving the Anm model, such as developing a new shell algorithm that has the ability to add shells of larger volumes.

2.7 Author Justifications

The research presented in this justification was a collaborative effort by Stephen Thomas, Dr. Yang Lu and Dr. E. J. Garboczi. Stephen took the responsibility of the lead author since he had the responsibility of preparing the code, testing it, performing the simulations and manuscript writing. Dr. Lu and Dr. Garboczi contributed to the research with detailed discussions and in-depth constructive feedback during the code development, simulation preparation, manuscript drafting and editing. Stephen Thomas's

research contribution was a partial fulfilment of the requirements for a Master of Science degree in Materials Science and Engineering at Boise State under the advisement of Dr. Yang Lu.

2.8 References

Aïtcin, P.-C. (1998). High-performance concrete, E&FN Spon, NewYork.

Alexander, M. G., and Mindess, S. (2005). Aggregates in concrete, Taylor & Francis, New York.

Amirjanov, A., and Sobolev, K. (2008). "Optimization of a computer sim- ulation model for packing of concrete aggregates." Part. Sci. Technol., 26(4), 380–395.

Arfken, G. B. (1970). Mathematical methods for physicists, Academic, New York.

Ayala, D., Brunet, P., Juan, R., and Navazo, I. (1985). "Object representation by means of nonminimal division quadtrees and octrees." ACM Trans. Graph., 4(1), 41–59.

Bentur, A., Alexander, M. G., and Comm, R. T. (2000). "A review of the work of the RILEM TC 159-ETC: Engineering of the interfacial transition zone in cementitious composites." Mater. Struct., 33(2), 82–87.

Bentz, D. P., Garboczi, E. J., Bullard, J.W., Ferraris, C. F., and Martys, N. S. (2006). "Virtual testing of cement and concrete." Significance of tests and properties of concrete and concrete-making materials, J. Lamond and J. Pielert, eds., ASTM, West Conshohocken, PA.

Bergen, G. V. D. (1997). "Efficient collision detection of complex deformable models using AABB trees." J. Graph. Tools, 2(4), 1–13.

Boon, C. W., Houlsby, G. T., and Utili, S. (2012). "A new algorithm for contact detection between convex polygonal and polyhedral particles in the discrete element method." Comput. Geotech., 44, 73–82.

Bradshaw, G., and O'sullivan, C. (2004). "Adaptive medial-axis approximation for sphere-tree construction." ACM Trans. Graph., 23(1), 1–26.

Bullard, J. W., and Garboczi, E. J. (2006). "A model investigation of the influence of particle shape on portland cement hydration." Cem. Concr. Res., 36(6), 1007–1015.

Cooper, D. W. (1988). "Random-sequential-packing simulations in three dimensions for spheres." Physical Rev. A, 38(1), 522–524.

De Larrard, F. (1999). Concrete mixture proportioning: A scientific approach, CRC Press.

Dewar, J. D. (1999). Computer modelling of concrete mixtures, E & FN Spon, New York.

Erdoğan, S. T., Garboczi, E. J., and Fowler, D.W. (2007). "Shape and size of microfine aggregates: X-ray microcomputed tomography vs. laser diffraction." Powder Technol., 177(2), 53–63.

Garboczi, E. J. (2002). "Three-dimensional mathematical analysis of particle shape using X-ray tomography and spherical harmonics: Application to aggregates used in concrete." Cem. Concr. Res., 32(10), 1621–1638.

Garboczi, E. J., and Bullard, J. W. (2013). "Contact function, uniform- thickness shell volume, and convexity measure for 3D star-shaped random particles." Powder Technol., 237, 191–201.

Garboczi, E. J., Cheok, G. S., and Stone,W. C. (2006). "Using LADAR to characterize the 3-D shape of aggregates: Preliminary results." Cem. Concr. Res., 36(6), 1072–1075.

Gebali, F. (2011). "Algorithms and parallel computing." Wiley, Hoboken, NJ.

Goldasteh, I., Ahmadi, G., and Ferro, A. (2012). "A model for removal of compact, rough, irregularly shaped particles from surfaces in turbulent flows." J. Adhes., 88(9), 766–786.

Jiménez, J. J., and Segura, R. J. (2008). "Collision detection between complex polyhedra." Comput. Graph., 32(4), 402–411.

Koehler, E. P., and Fowler, D. W. (2007). Role of aggregates in self- consolidating concrete, International Center for Aggregates Research, Austin, TX.

Kwan, A. K. H., and Fung,W.W. S. (2009). "Packing density measurement and modelling of fine aggregate and mortar." Cem. Concr. Compos., 31(6), 349–357.

Kwan, A. K. H., and Mora, C. F. (2001). "Effects of various shape parameters on packing of aggregate particles." Mag. Concr. Res., 53(2), 91–100.

Lamond, J. F., and Pielert, J. H. (2006). Significance of tests and properties of concrete and concrete-making materials, ASTM, West Conshohocken, PA.

Lecomte, A., de Larrard, F., and Mechling, J. M. (2005). "Predicting the compressive strength of concrete: The effect of bleeding." Mag. Concr. Res., 57(2), 73–86.

Lu, Y., and Garboczi, E. (2014). "Bridging the gap between random micro- structure and 3D meshing." J. Comput. Civ. Eng., 10.1061/(ASCE)CP .1943-5487.0000270, 04014007.

Lu, Y., Garboczi, E., Bentz, D., and Davis, J. (2012). "Modeling chloride transport in cracked concrete : A 3-D image-based microstructure simulation." COMSOL Conf. 2012, Boston.

Max, N. L., and Getzoff, E. D. (1988). "Spherical harmonic molecular surfaces." IEEE Comput. Graph. Appl., 8(4), 42–50.

Mondal, P., Shah, S. P., and Marks, L. D. (2009). "Nanomechanical properties of interfacial transition zone in concrete." Nanotechnology in construction, Z. Bittnar, P. M. Bartos, J. Němeček, V. Šmilauer, and J. Zeman, eds., Springer, Berlin, 315–320.

Neville, A. M. (2011). Properties of concrete, Pearson, New York.

Ollivier, J. P., Maso, J. C., and Bourdette, B. (1995). "Interfacial transition zone in concrete." Adv. Cem. Based Mater., 2(1), 30–38.

Qian, Z. (2012). "Multiscale modeling of fracture processes in cementitious materials." Delft Univ. of Technology, Netherlands.

Qian, Z., Garboczi, E. J., Ye, G., and Schlangen, E. (2014). "Anm: A geometrical model for the composite structure of mortar and concrete using real-shape particles." Mater. Struct., in press.

Rauber, T. R. G. (2010). Parallel programming: for multicore and cluster systems, Springer, Berlin.

Shane, J. D., Mason, T. O., Jennings, H. M., Garboczi, E. J., and Bentz, D. P. (2000). "Effect of the interfacial transition zone on the conductivity of portland cement mortars." J. Am. Ceram. Soc., 83(5), 1137–1144.

Sobolev, K., and Amirjanov, A. (2004). "The development of a simulation model of the dense packing of large particulate assemblies." Powder Technol., 141(1–2), 155–160.

Subhlok, J., Stichnoth, J. M., O'hallaron, D. R., and Gross, T. (1993). "Exploiting task and data parallelism on a multicomputer." ACM SIGPLAN Notices, 28(7), 13–22.

Xie, H. Q., Fujii, M., and Zhang, X. (2005). "Effect of interfacial nanolayer on the effective thermal conductivity of nanoparticle-fluid mixture." Int. J. Heat Mass Transfer, 48(14), 2926–2932.

Xu, W., Chen, W., Chen, H., Tian, X., and Zhao, H. (2014a). "Determination of overlapping degree of interfacial layers around polydisperse ellipsoidal particles in particulate composites." Phys. A Stat. Mech. Appl., 399, 126–136.

Xu, W. X., Chen, H. S., Chen, W., and Jiang, L. H. (2014b). "Prediction of transport behaviors of particulate composites considering microstructures of soft interfacial layers around ellipsoidal aggregate particles." Soft Matter, 10(4), 627–638.

CHAPTER THREE: IMPLICATIONS OF OVERLAPPING UNIFORM-THICKNESS

SHELLS IN THE ANM MODEL

3.1 Introduction

As outlined in Chapter 1, the introduction of overlapping uniform thickness shells will significantly broaden the scope of the Anm model. The particle parking algorithm and the data visualization is adapted because unlike the previous version where the uniform thickness shell was not included in the final model, the shells need to be visualized along with the actual particles in the new version. Two potential challenges are identified as follows:

(1) Since the shell and particle are hard to distinguish in the visualization, there must be some means to tell them apart. The input and output specifications need to be adapted to meet these needs.

(2) Even if some means of distinguishing the particles and shells is devised, visualizing it in 3D will be a challenge even with translucent shells.

The identified solution to the first problem is to assign different colors to each layer of shells added to the particles and to modify the output file format to allow the shells and particles to be treated separately for post-processing or visualization. To address the second problem, the capability of producing 2D slices of the 3D model is added to the Anm model. Images with custom resolution can be generated from any location within the model with this new feature. The method for generating 2D slices with overlapping shells is described in the remaining part of this chapter along with an

important application of this new feature. The application of the 2D slicing described here is a method to characterize the so called "wall effect" observed in concrete using the Anm model.

3.2 Overlapping Uniform Thickness Shell

The existing algorithm for adding uniform thickness shell to a single particle is used without any changes for overlapping shells. However, the particle parking algorithm needs to be carefully redesigned for this feature. In the previous version where non-overlapping shells were assumed, the shells were added to every particle that could be parked without overlapping with any other particle, and rechecked if the shell overlapped with any other particles. If both conditions were satisfied, the original particle was retained. In a densely-packed specimen, this step turns out to be a time intensive step in the algorithm. This is because there will be many cases where the new particle does not overlap with other existing particles, but the shell does overlap and hence the original particle cannot be retained and a new particle placement attempt must be performed. This step is shown in Fig. 3.1 with dashed lines.
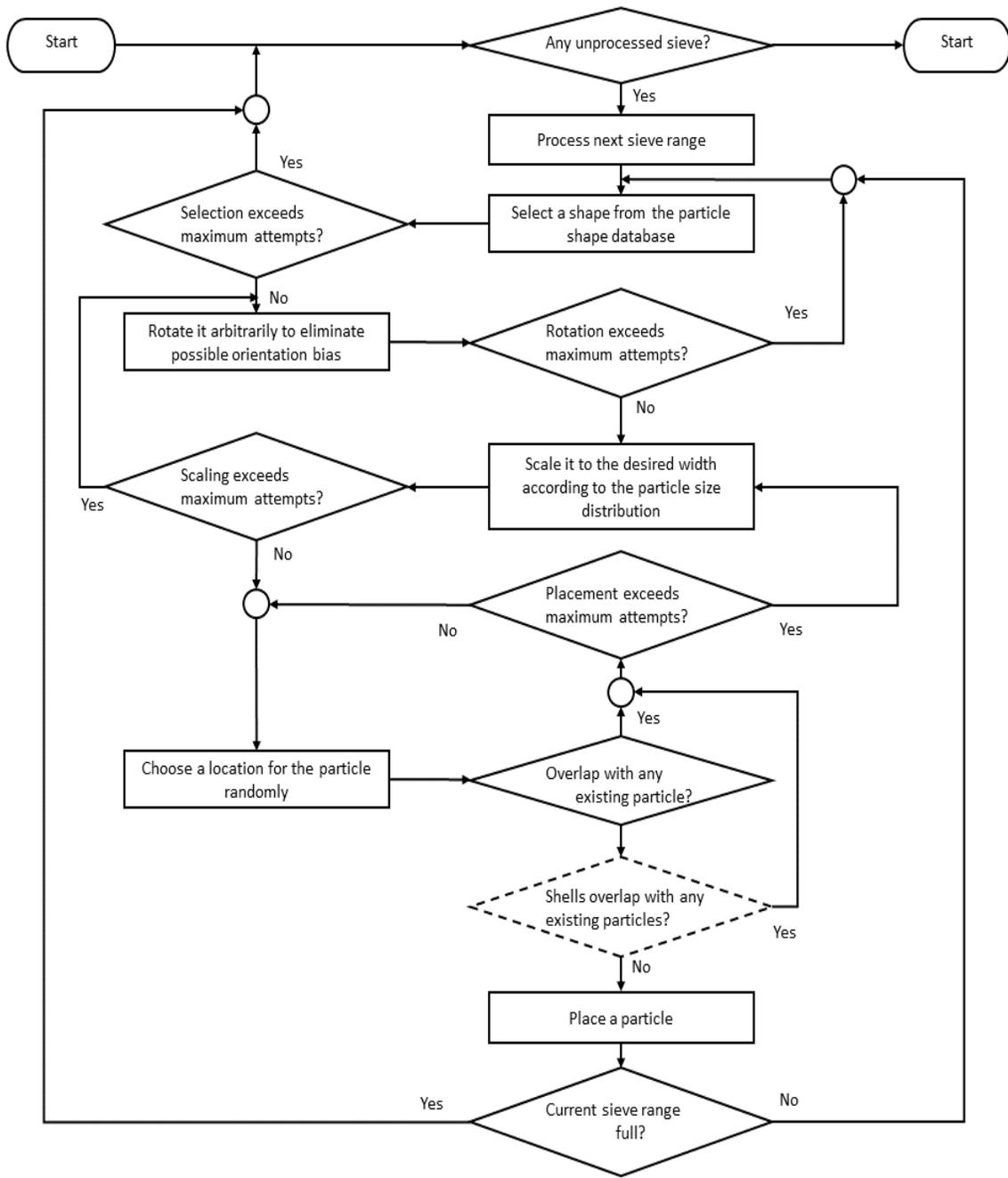
Fig. 3.1. **Flowchart for parking procedure with non-overlapping shells.**

However, this step is not necessary during the parking progress for overlapping shells and only the particles need to be checked for contact with other existing particles. An important consideration for visualizing the Anm model is the memory requirement for densely packed models. If the size of the particles relative to the volume containing them

is large, the resolution of the particle shape is more important aesthetically than particles which are relatively much smaller than the containing volume. For instance, in a three-phase concrete model, the size of aggregates and cement grains are three orders of magnitude apart. Using a lower resolution for the cement grain will greatly reduce the memory requirement of the visualization without affecting the aesthetics. Even with reduced resolution for smaller particles, it has been found that the Anm model with more than a few thousand particles becomes too large to visualize on standalone desktop or laptop computers with limited memory resources and require distributed rendering capabilities using cluster computing facilities. The addition of overlapping shells makes this problem even worse. A provision has been added to the model to skip adding overlapping shells to all the particles during packing and instead add the shells to just the particles that are part of a 2D slice. The 2D slicing method explained in the next section has been identified as a viable option to post process or visualize models which are not feasible to visualize in 3D due to memory constraints.

In this variation of the Anm model, the particles do not overlap each other, but the shells can overlap other shells as well as other particles. This may not seem like a physically relevant scenario, but turns out to be a useful starting point as shown in the next section. User-defined colors specified for each shell layer in the input file are used to color-code the shells. The output file which is of VRML format (Carey and Bell, 1997) can either be a single file containing all the particles and shells, or it can be saved separately where all the particles are saved in one file and shells from each layer are saved in separate files. This will enable easy switching on and off a certain layer of the shell for all the particles at once.

3.3 2D Slicing and Visualization of The Anm Model

Given that there can be one or more shells for each particle and the shell thickness is only marginally larger than the actual particle itself, visually analyzing the generated model in 3D can be a daunting task. The fact that visualization is usually done on a 2D screen compounds the problem. The difficulty of analyzing the 3D data presents itself even for computational analysis. Analyzing 2D representations in the form of slice images is proposed as a more viable option for both visual and computational analysis. For example, if some statistical measurement needs to performed within each layer, it might be possible to perform this measurement of the slices with preferred resolution and finally add up the individual slice measurements to get the 3D equivalent measure.

Consider a particle with two uniform thickness shells added to it. Then the first shell can be called the inner shell and the second shell can be called the outer shell. For the purpose of these discussions it is assumed that the volume between the inner shell surface and the particle surface is classified as the volume occupied by the inner shell and the volume between the outer shell surface and the inner shell surface is the volume occupied by the outer shell. The procedure for generating the 2D slice starts with defining the slice rectangle. The slice rectangle is constrained to be two dimensional and at least one of the dimensions must have a thickness of 0. However, it will be interesting to see what kind of measurements may benefit from having a finite thickness slice rectangle for which the data for each pixel in the resultant image would represent a statistical measure such as a mean along the direction normal to the slice plane. Each particle in the generated model is then checked for contact with the slice rectangle using a very similar method as the EOB method described in Chapter 1 and 2. In this scenario,

the extent box needs to be computed for the single particle in question and the other extent box is the slice rectangle which is flat (thickness of 0) along one of the dimensions. The limitations of the EOB method in terms of the limits imposed by $N_{ext,}$ is applicable for this method also. Consequently, the recommendations for the optimum value of N_{ext} stated in Section 2.5.1 may be followed for this method. Once the EOB is detected for a particle, the distance from each pixel position in the slice to the particle center is measured (O to p1 and O to p2 in Fig. 3.2). If this distance is more than the distance from the center of mass of the particle to the surface, the particle is classified as not overlapping the slice plane at that pixel position in the slice. In Fig. 3.2, the slice is parallel to the y-z plane and an EOB is detected. Position p1 in the slice is overlapped by the particle and position p2 is not overlapped.
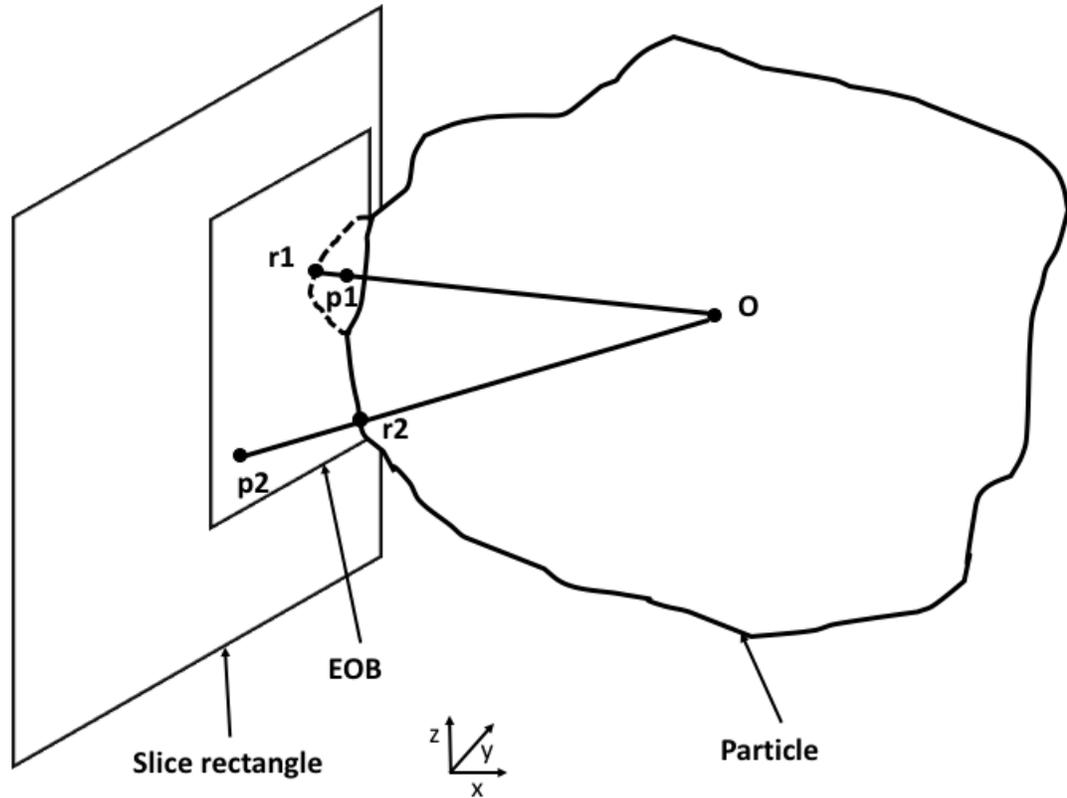
Fig. 3.2 **Schematic of a particle-slice overlap. Position p1 on the slice is overlapped by the particle. The dotted line shown part of the particle behind the slice. Position p2 is not overlapped by the particle. r1 and r2 are surface points on the surface of the particle along the direction of points p1 and p2.**

Like the interparticle contact detection method, this scan is only performed within an angle range given by the EOB extents in the two directions parallel to the slice plane, but the coarseness of the scan is governed by the image resolution parameter I_{res} which is given by dividing the slice rectangle dimension by the corresponding 3D volume dimension. If the pixel position is found to be overlapping with a particle or a shell, a corresponding label value is assigned to the pixel. To model physical phenomenon such as the ITZ layers in concrete, a few constraints were imposed while labelling the pixels:

(1) A pixel position overlapped by a particle and a shell is labelled as particle.

(2) A pixel position overlapped by different shells from the same layer hierarchy gets labelled as that layer without any ambiguity.

(3) A pixel position overlapped by a shell from two different layer hierarchies gets labelled as the inner layer.
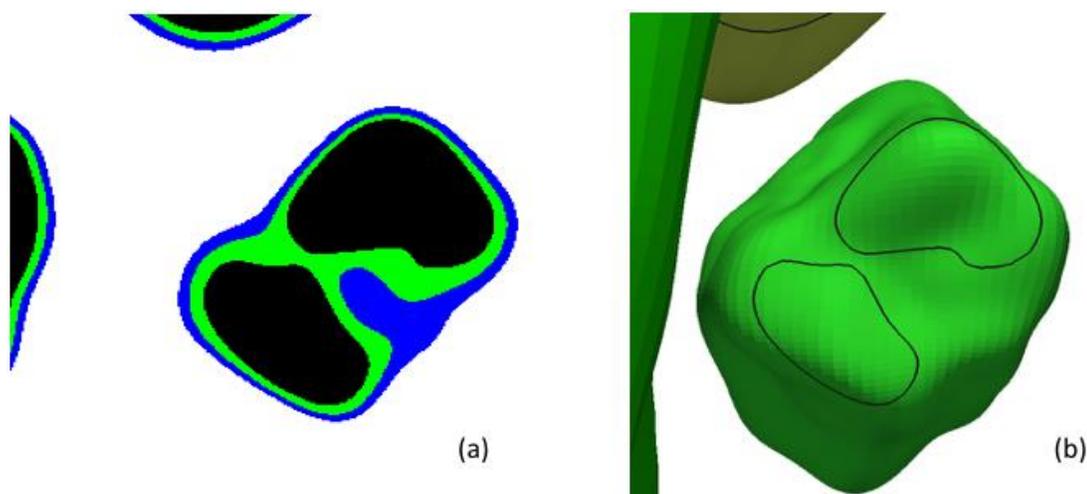
Fig. 3.3. **2D slice image of overlapping shells obtained from the Anm model (a) and the corresponding particles and slice (shown as the black curve) in 3D (b).**

This set of constraints can give rise to 2D slices as shown in Fig. 3.3. The black color in the 2D slice image (left) represents the particle and the green color represents the inner shell and the blue represents the outer shell. The corresponding region in the 3D Anm model is also presented on the right side of Fig 3.3 to clearly visualize the effect of slicing. The two apparently separate particles on the bottom-right side of the 2D slice are actually a single particle and this becomes obvious in the 3D visualization. Both inner and outer shells of the two apparently separate particles in the 2D slice appear to coalesce to form a single connected phase because of the constraints imposed on the pixel labelling.
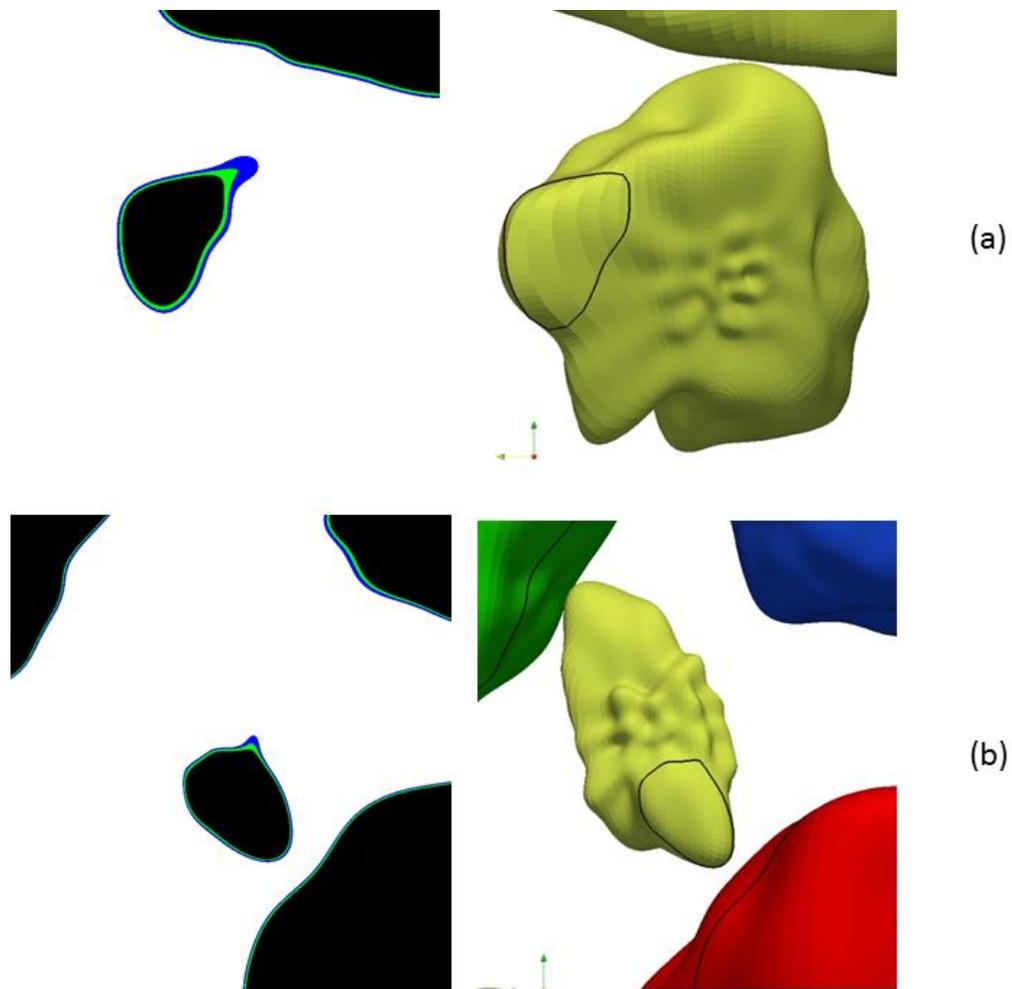
Fig. 3.4. **2D slice image of varying thickness of the shells on high angle slice planes obtained from the Anm model (left) and the corresponding particles and slice (shown as the black curve) in 3D.**

Another interesting observation from the 2D slice analysis of the Anm model is

the apparent thickness of the uniform thickness shell and how it varies based on the angle

with which the slice plane intersects the particle and shells. This is clearly visible in Fig

3.4 where two different slices (a) and (b) are presented with the slice image on the left

and the corresponding 3D visualization on the right. A protrusion in the shell can be

observed in the slice image on both Fig 3.4 (a) and (b). This increase in apparent

thickness is attributed to the high angle between the slice plane and the surface normal.

One study estimated the increase in the apparent thickness of the ITZ to be an average "lengthening factor" of 1.2 (Crumbie, 1994).

3.4 Characterizing the wall effect

It is well known that the porosity around aggregates tend to be higher than the bulk porosity in concrete and this effect is often referred to as the "wall effect" in the ITZ (Bentz, Garboczi and Stutzman, 1993). The "wall effect" is an experimentally observed phenomenon that affects the packing density of fine aggregates and sand near the surface of coarse aggregates. This is purely a geometric effect and can be understood well from Fig. 3.5.
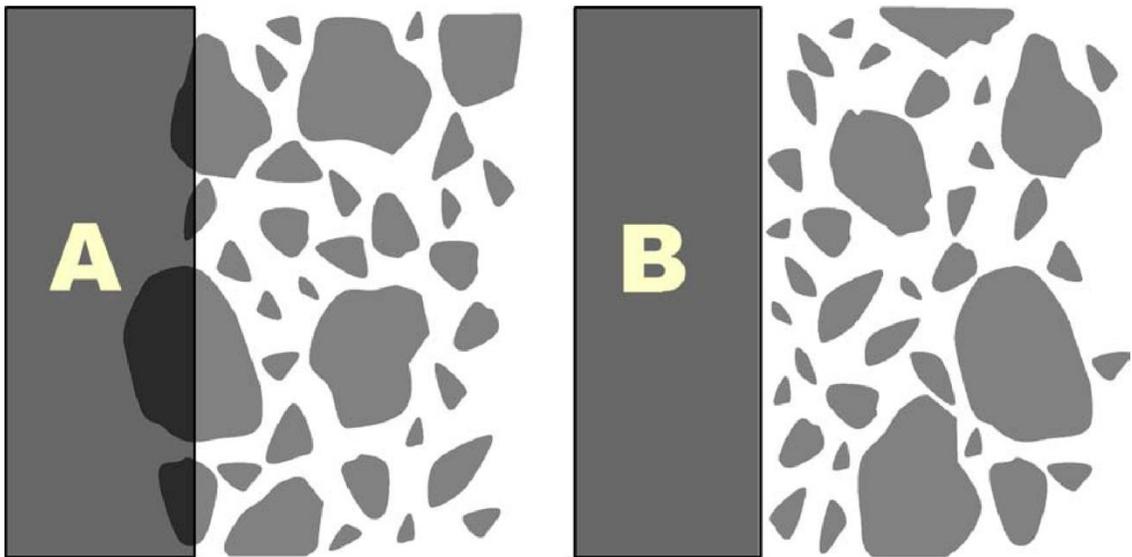
Fig. 3.5. **Illustration of the "wall effect". A is a penetrable wall and B is an impenetrable wall. The packing density near wall B is lower than wall A. (Scrivener, Crumbie and Laugesen, 2004)**

The extent of this low-density region is critical to the mechanical strength of concrete and is therefore important to characterize. Experimentally, the average packing density in the low-density region can be characterized by analyzing the backscattered electron (BSE) images of polished sections of concrete samples (Scrivener, Crumbie and Laugesen, 2004). One of the challenges of this technique is measuring the normal

distance from the aggregate surface in 2D sections. This problem is related to the apparent increase of the uniform thickness shell discussed in the previous section. Calculating the extent of the wall effect from the 3D Anm model will involve scanning the density around each coarse aggregate with a predefined resolution and averaging the obtained packing densities. Measuring this quantity from 2D slices is a more tractable solution to this problem.

One such measured property of the 3D Anm model is the packing fraction of the specimen ($\emptyset_p$) which depends on the aggregate shape, particle size distribution and simulation time. $\emptyset_p$ can be expressed as shown in Equation 3.1 where V_p is the volume occupied by the particles and V_Ω is the volume occupied by the specimen. In the context of the Anm model V_Ω constitutes the volume of aggregates (V_a), volume occupied by the small particles (V_s) which could be sand particles or cement particles and volume of the matrix (V_m) which is the empty space in the Anm model.

$$\emptyset_p = \frac{V_p}{V_\Omega} \qquad\qquad 3.1$$

$$V_\Omega = V_p + V_m \equiv V_a + V_s + V_m \qquad\qquad 3.2$$

In 2D slices obtained from the Anm model, the exact extent of the uniform thickness shell is known in all directions and density of particles within this region can be measured with an accuracy limited by the resolution of the slice images. A very similar concept found in crystallography is the radial distribution function (RDF) which essentially measures the number density of atoms around each atom as a function of the distance from itself. The RDF provides useful information such as the first nearest-neighbor distance and second nearest neighbor distance. Visual inspection of the RDF

can be used to understand whether the material is crystalline or amorphous. The RDF of crystalline materials tend to exhibit characteristic peaks whereas for amorphous materials the peaks are not seen away from the origin. The area under the RDF from zero to the first nearest neighbor peak gives the coordination number of the structure.

An attempt is made in this research to represent the distribution of smaller particles near the surface of the coarse aggregates as an RDF and explore the useful information that can be extracted from it. This approach provides a method to characterize the "wall effect" seen in concrete. The smaller particles may be assumed to be sand particles or cement particles depending on the chosen size scale. The factors that can affect the RDF of the Anm model are hypothesized as (1) the coarse aggregate shape and (2) the packing fraction ($\emptyset_p$). The low-density region near the aggregate surface in the Anm model cannot simply be equated with the ITZ zone which is a dynamic region that changes based on other factors such as temperature, water to cement ratio and age (Haecker et al., 2005; Zheng, Wong, & Buenfeld, 2009).

The first factor can be tested by comparing the RDF of aggregate shapes that have very different shape characteristics. A previous study (Xu, Lv and Chen, 2013) using polydispersed ellipsoidal particles placed near flat walls have shown that shape does not contribute significantly to the wall-effect. However, $\emptyset_p$ is influenced by the particle shape and the particle size distribution of the system. Hence the effect of $\emptyset_p$ on the RDF can be studied to relate the PDS and particle shape to the RDF indirectly. Apart from the two model characteristics, numerical factors such as the resolution of the slice image (R_s) and the slice density (ρ_s) should also be considered while characterizing the RDF. The R_s units considered in the Anm model is typically mm/pixels. ρ_s is unit less and is given by

Equation 3.3 where N is the number of slices and N_{max} is the maximum number of slices

and $N \leq N_{max}$ such that $0 \leq \rho_s \leq 1$. There is no limit on the maximum number of

slices, but it is convenient to let N_{max} correspond to the value of R_s so that the imaginary

voxels formed by putting together the slices will be cubic in shape. Then N_{max} is given

by Equation 3.4 where X_{max} and X_{min} are the extents of the slicing along the axis normal

to the slice plane.

$$\rho_s = \frac{N}{N_{max}} \qquad 3.3$$

$$N_{max} = \frac{X_{max} - X_{min}}{R_s} \qquad 3.4$$

The slice density controls the frequency with which the specimen is sampled by

slicing. These two numerical factors are important because 2D slices of the 3D model are

used to measure the RDF as an averaged quantity. A higher image resolution (lower R_s)

for the 2D slices results in a more accurate density calculation. Very low resolution slice

images can result in missing particles in the image. A low slice density in a less densely

packed specimen can result in a set of slices that does not sample the ITZ layer

sufficiently. As the slice density increases, the resulting RDF is expected to converge for

a given sample when the amount of sampling is sufficient to produce an averaged value

which does not vary with more dense sampling.

The RDF described here considers $t \equiv t.\hat{n}$, the normal distance from the surface

as the independent variable and $g(t)$ as the dependent variable where $g(t)$ is a unit less

quantity representing the ratio of packing fraction at a distance t from the surface to the

packing fraction of the matrix described in Equation 3.6. Typically, the RDF uses

distance from the center of a particle (r) as the independent variable. But, in this context

t is used because it denotes the thickness of the uniform thickness shell or distance from the surface of the particle.

The formulation of $g(t)$ is detailed here. Consider a cubic Anm model called M_{sand} with sides of length 20 mm, coarse aggregates occupying V_a and sand particles occupying V_s. Also, consider a volume called "bulk volume" (V_B) which is the volume that excludes the coarse aggregates. Then,

$$V_\Omega = V_a + V_B = V_a + (V_s + V_m) \Rightarrow V_B = V_\Omega - V_a . \qquad 3.5$$

This space has a packing fraction called the bulk packing fraction (ϕ_B) which is given by Equation 3.6.

$$\phi_B = \frac{V_s}{V_B} = \frac{V_s}{V_\Omega - V_a} . \qquad 3.6$$

The "wall-effect" idea proposes that at $t = 0$, the local packing fraction is zero and increases with t and eventually reaches ϕ_B. $g(t)$ is defined such that the local packing fraction is given by $g(t).\phi_B$. Then, as the local packing fraction approaches the ϕ_B, $g(t)$ approaches 1.

However, in this research, $g(t)$ is not calculated directly from the 3D Anm model. Instead, many 2D slices are analyzed and assumed to be equivalent to the 3D measurements. Consider a group of N slices which is equivalent to M_{sand} described above. Let R_s be 0.05 mm/pixel and consequently, N_{max} is 400. The area of an individual slice i is denoted as A_i where $i \in N$ and $A_i = A^m + A^a + A^s$ where the notations are consistent with the volume counterparts. Let the number of uniform thickness shells in M_{sand}, be K and $K = 10$. Then the area occupied by an individual shell j in the i slice

can be denoted as A_{ij}. Since we assume the equivalence between the 3D volume and N

slices, the volume of the j shell in the 3D model (V_j^{shell}) is given by

$$V_j^{shell} = \sum_i^N A_{ij}, \qquad when\ N \to \infty \qquad\qquad 3.7$$

The area fraction occupied by sand particles in the ith slice (φ_i^s) is given by

Equation 3.8 where A_i^s is the area occupied by sand particles in the ith slice.

$$\varphi_i^s = \frac{A_i^s}{A_i} \qquad . \qquad\qquad 3.8$$

The area fraction occupied by sand in the jth shell in the ith slice is given by

Equation 3.9.

$$\varphi_{ij}^s = \frac{A_{ij}^s}{A_{ij}} \qquad . \qquad\qquad 3.9$$

So far, only quantities in individual slices were considered. The quantity of

interest of this study is the average packing fraction of sand in the jth shell of all the N

slices which is given by Equation 3.10.

$$\varphi_j^s = \frac{\sum_i^N A_{ij}^s}{\sum_i^N A_{ij}} . \qquad\qquad 3.10$$

When N is sufficiently large, Equation 3.11 is true. Care must be taken to avoid

very small N such that there are no slices which cut through the jth shell such that the

denominator of Equation 3.10 is zero. $\varphi_j^s \equiv \varphi_j^s(t)$, since the area of the slice is

dependent on the thickness of the uniform thickness shell. Equation 3.11 is one of the

important conclusions of this section and the remainder of this section expects to

numerically show this equality.

$$\frac{\varphi_j^S}{\phi_B} = g(t) \quad . \qquad 3.11$$

Since $g(t)$ is calculated as an averaged quantity from N slices, the standard

deviation of this quantity is used to determine the optimum number of slices.

The numerical factors to be considered for calculating the RDF are explored now.

An Anm model described before as M_{sand} is generated with the PSD described in Table

3.1. The order of Anm coefficients used is 14 for Sieves 1 and 2. The order of Anm

coefficients used for Sieve 3 is 5 to achieve better performance. It is assumed that the

detailed shape of the sand particles will be less significant compared to the shape of the

much larger coarse aggregates. The ϕ_p of the model is ~ 23%. 2D slices are generated

normal to the x-axis where the images have 400 pixels each in the y-axis and z-axis.

Thus, the R_s is 0.05 mm/pixel and N_{max} is 400 when the range of the slicing extent is the

extent of the simulation box.

Table 3.4 **PSD and achieved volume fraction by M_{sand}. The first column describes the minimum and maximum width of the particles in that sieve.**

Sieve #	Prescribed Volume Fraction	Achieved Volume Fraction	Packed Particles
Sieve 1 (9.9-10.0 mm)	0.20	0.13	2
Sieve 2 (4.9-5.0 mm)	0.02	0.02	3
Sieve 3 (0.15-0.25 mm)	0.08	0.08	202736

Fig 3.6 shows the particles from Sieves 1 (blue) and 2 (green). The particles from

Sieve 3 has been omitted from the visualization. The largest aggregate with a length of

9.997 mm is chosen to study the RDF of a single particle. This particle will be referred as

the RDF-particle. The RDF-particle is depicted in Fig. 3.6 with uniform thickness shells

around it, even though only the outer most shell (light blue) is visible. Ten uniform

thickness shells were generated for this particle with the thickness ranging linearly from

0.025 mm to 0.474 mm which corresponds to 0.5 to 5 % of the RDF-particle length. A

2D slice normal to the x-axis and passing through the RDF-particle is shown in Fig. 3.7.

The pixels representing the ten uniform thickness shells are assigned labels so that the

label image can be used as masks for measuring density of sand particles within each

shell. In Fig. 3.7, the shells are colored with pseudo colors and the mask image is

superimposed on the slice image for illustration.
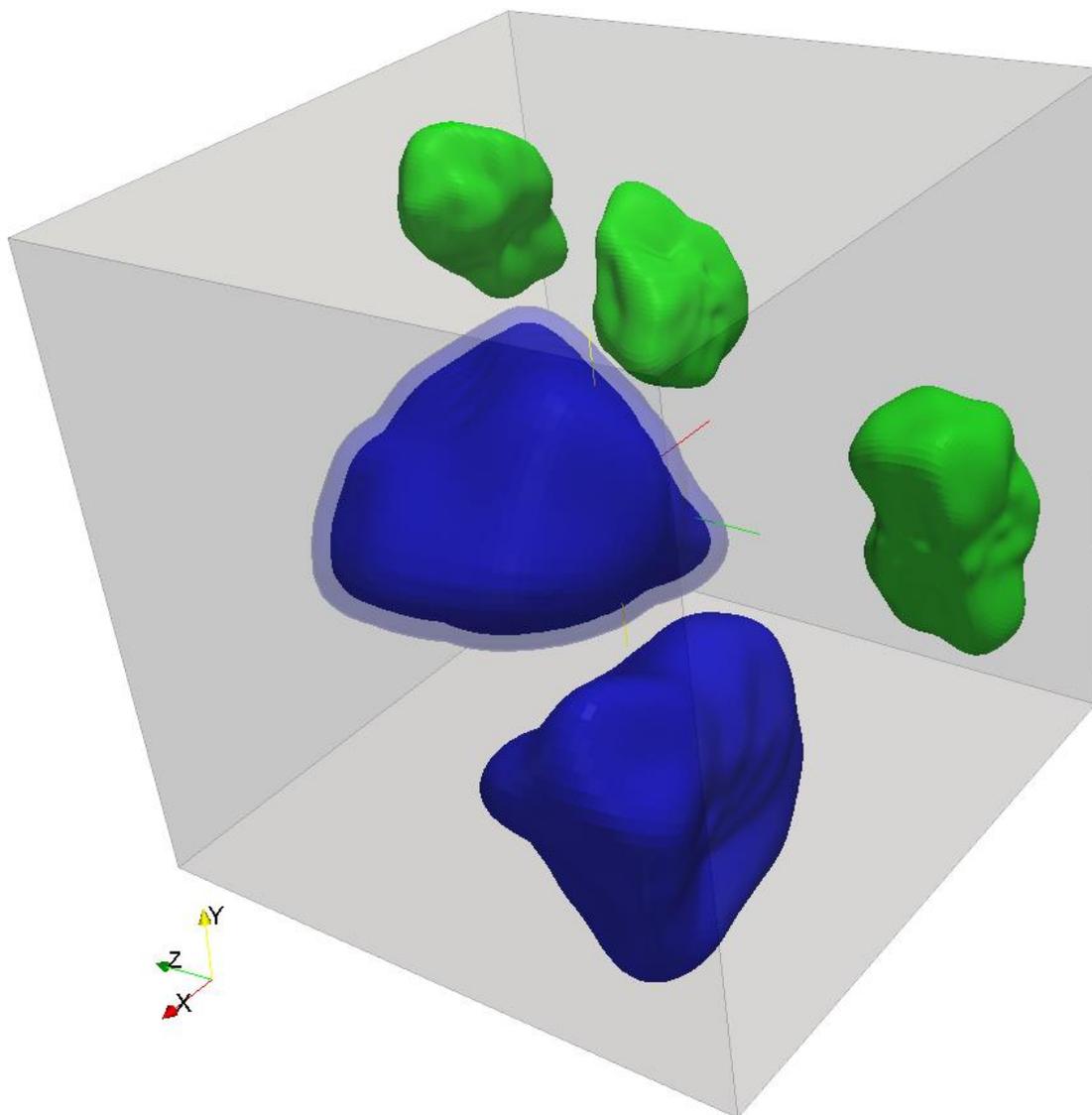
Fig. 3.6.   3D visualization of Anm model 1 where only particles from Sieve 1 (blue) and Sieve 2 (green) are shown. The particle for which the RDF is calculated is shown with the uniform thickness shell (light blue) around it.
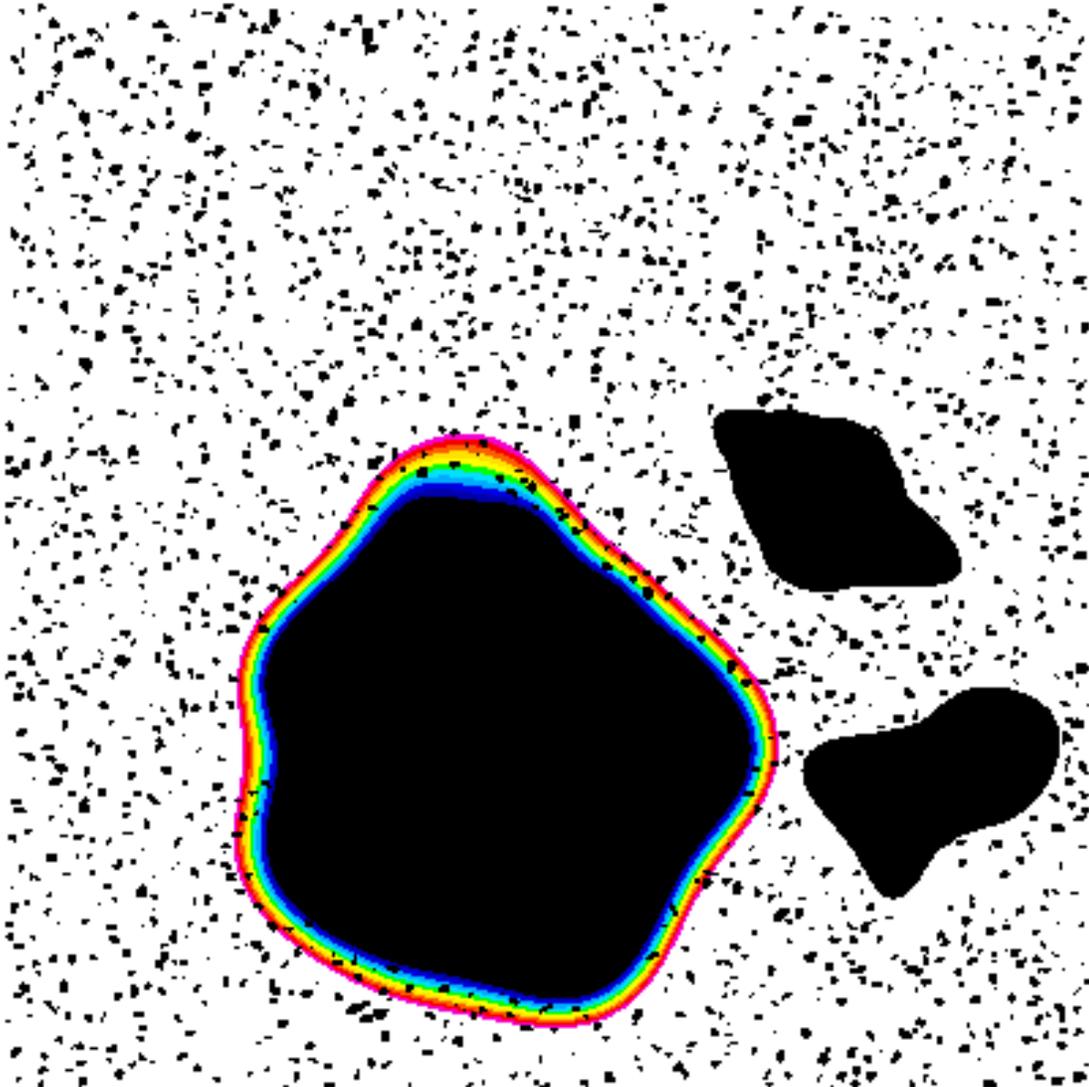
Fig. 3.7.   Illustration of a mask image superimposed on a corresponding 2D slice of the Anm model 1 passing through the coarse aggregate for which the RDF is measured. The ten uniform thickness shells are colored with pseudo colors and the particles are shown in black.

The $g(t)$ is calculated by performing pixel counting on slice images obtained at different slice densities. The pixel counting algorithm involves counting black pixels within the mask region for each shell. The area fraction occupied by the sand particles is then calculated by dividing the pixel count for sand particles by the pixel count for the corresponding shell mask. Once the area fraction is obtained for each shell for many slices, the mean and standard deviation is calculated. The RDF is plotted as shown in Fig. 3.8 where ϕ_B is obtained from Table 3.1 using Equation 3.6 as 0.09. The bar graph is

indicative of the fact that the RDF is calculated within each shell and the width of each

bar is the thickness of the uniform thickness shell used in the simulation. The error bar

indicates that the averaged g(t) is obtained from *N* slices.
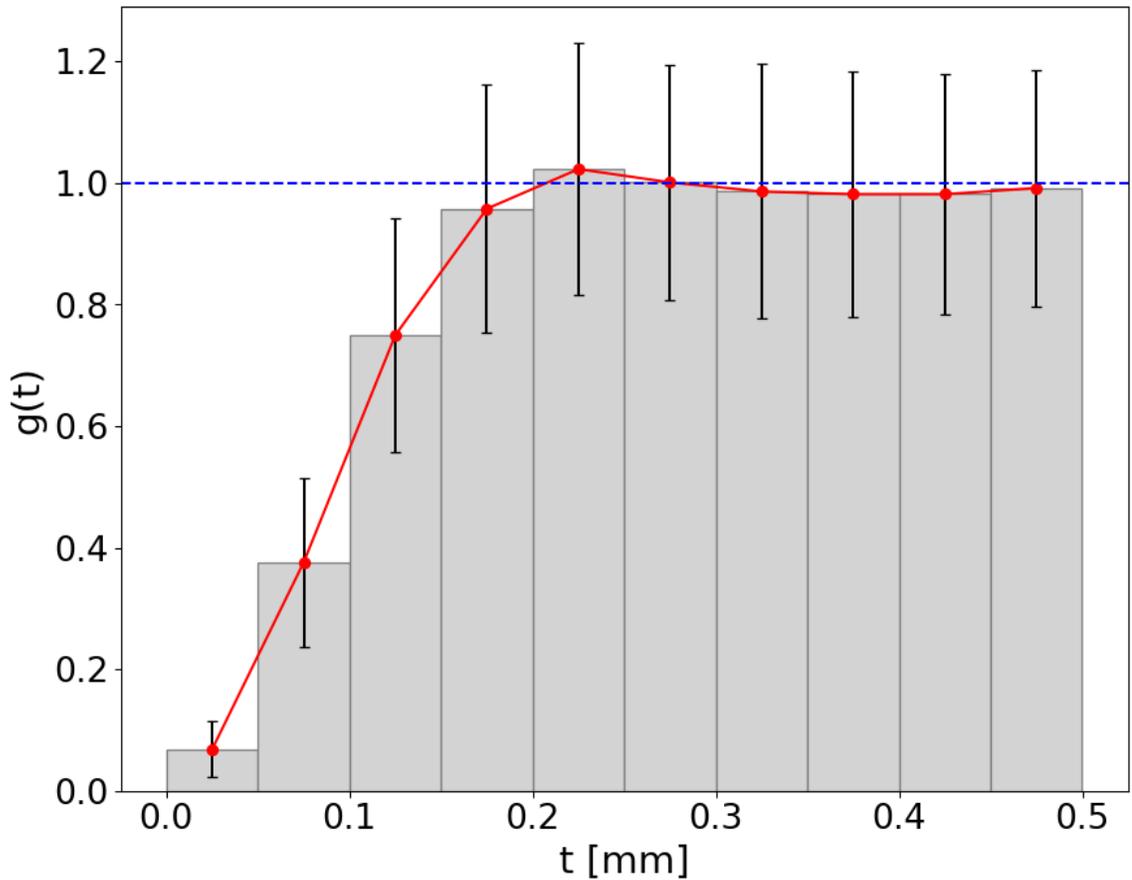
Fig. 3.8.   **The RDF calculated for one coarse aggregate with a slice density of 1.**

As expected, the density is lowest near the aggregate surface and increases as a

function of the distance from the particle surface. The sand density approaches ϕ_B at

around 0.2 mm from the particle surface and fluctuates about ϕ_B beyond that distance

from the surface. From Fig 3.7, it can be deduced that the low-density region extent for

M_{sand} is ~0.175 mm. However, previous studies suggests that the ITZ has a thickness

less than 0.040 mm (Scrivener, Crumbie and Laugesen, 2004). It is important to note that

M_{sand} does not explicitly consider cement grains. Including cement grains in the model

may increase the ϕ_B. It is also reasonable to expect a thinner porous region in such a model.

The high standard deviation is expected because of the low ϕ_B (~9%). Another possible reason for the high standard deviation could be the proximity of other particles to the RDF-particle. Due to this reason, slices with neighboring particles near the RDF-particle will have a lower density than slices without such neighboring particles. This deviation cannot be avoided with higher sampling density. This concern may not be real for models with higher ϕ_B and a thinner porous region.
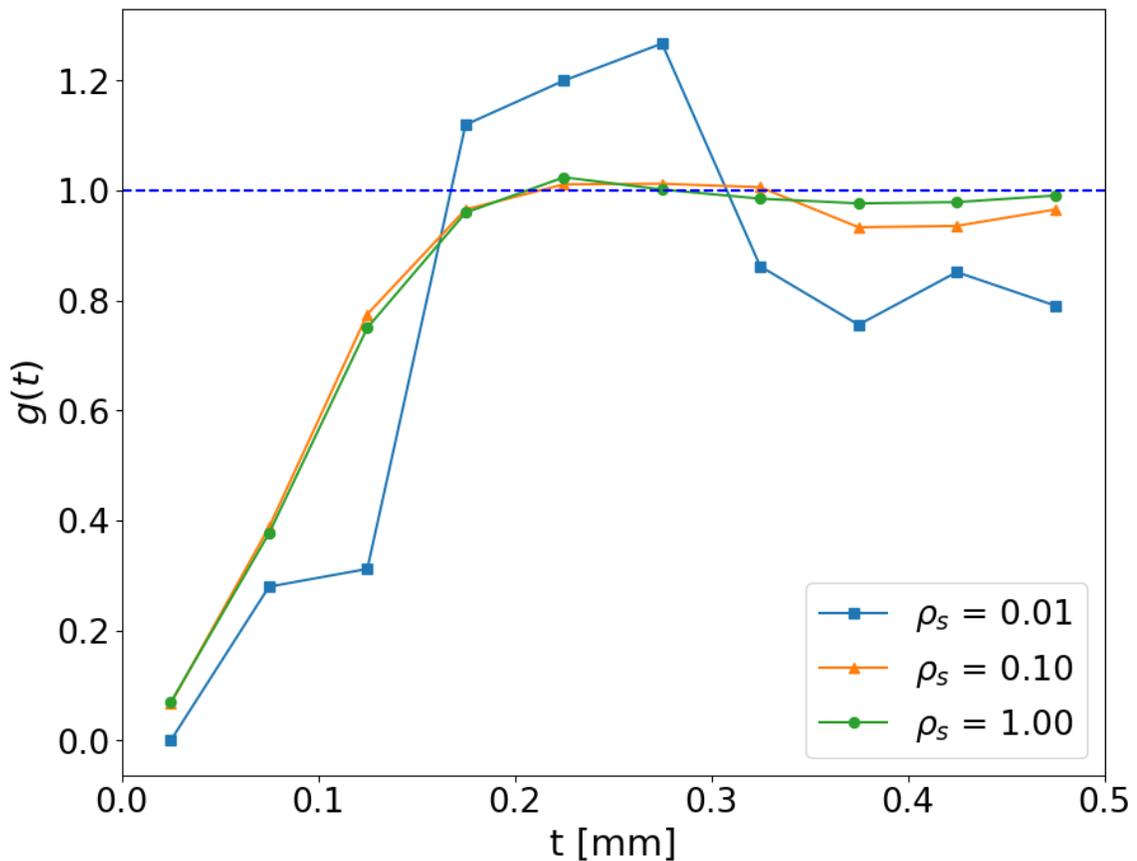
Fig. 3.9. **The RDF calculated for one coarse aggregate with four different slice densities. Slice density of 1 corresponds to R_s of 0.05 mm/pixel.**

Fig. 3.9 shows how the RDF varies with three different slice densities (ρ_s). The lowest ρ_s plot corresponds to two slices which cut through the outer shells only on

opposite extremes of the particle along the x-axis. The RDF computed with a lower ρ_s

shows large deviations from the bulk density at larger values of t. compared to the RDF

computed using ρ_s of 1. The minimum number of slices necessary to reduce the standard

deviation to a minimum is studied by taking four distances from the surface (t) of the

particle and considering the variation in the standard deviation of $g(t)$ as a function ρ_s as

shown in Fig. 3.10.
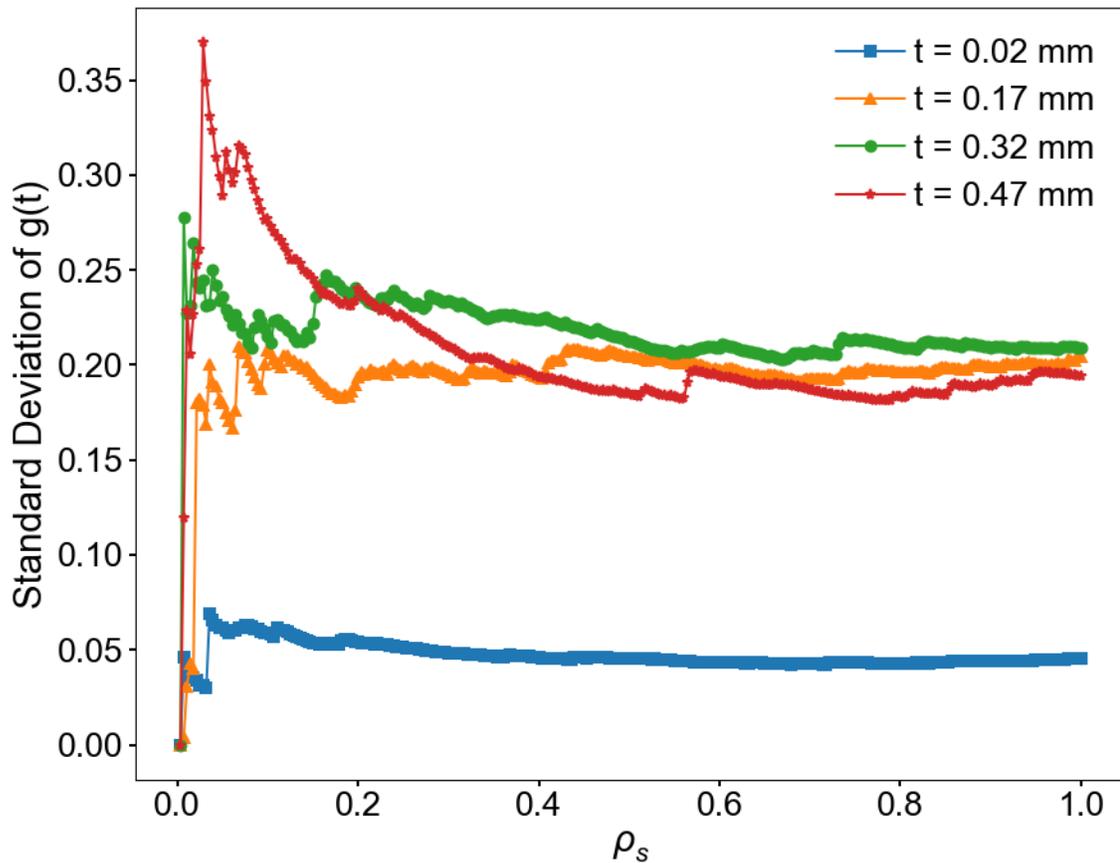
Fig. 3.10. **Variation in standard deviation of the RDF with increasing slice density(ρ_s).**
Four distances from the particle surface is considered. Slice density of 1 corresponds to R_s of
0.05 mm/pixel.

The inner shells corresponding to the blue curve ($t = 0.02\ mm$) appears to

experience the least standard deviation. The standard deviation of the outer most shell

shows very large standard deviations at low ρ_s. This might be because of the wall effect

caused by the neighboring aggregates as seen in Figures 3.5 and 3.6. All the four curves

appear to be converging at $\rho_s \sim 0.5$. For the given Anm model, it can be concluded that a

ρ_s of 0.5 is sufficient to calculate the RDF. This conclusion is justified further by

observing in Fig. 3.9 that even for $\rho_s = 0.1$, the RDF shows very little variation from the

RDF for $\rho_s = 1$. The particles in sieve 3 can be optimized for performance by assuming

spherical shape. This is achieved by reducing the order of Anm coefficients from 5 to 0.

Table 3.2 describes the packing density achieved using this optimization and Fig. 3.11,

3.12 and 3.13 shows the RDF data computed for resultant model.

Table 3.2 **PSD and achieved volume fraction by M_{sand} where particles from Sieve 3 were assumed to be spherical particles by reducing the order of Anm coefficients used to 0 instead of 5. The first column describes the minimum and maximum width of the particles in that sieve.**

Sieve #	Prescribed Volume Fraction	Achieved Volume Fraction	Packed Particles
Sieve 1 (9.9-10.0 mm)	0.20	0.13	2
Sieve 2 (4.9-5.0 mm)	0.02	0.02	3
Sieve 3 (0.15-0.25 mm)	0.08	0.08	202852
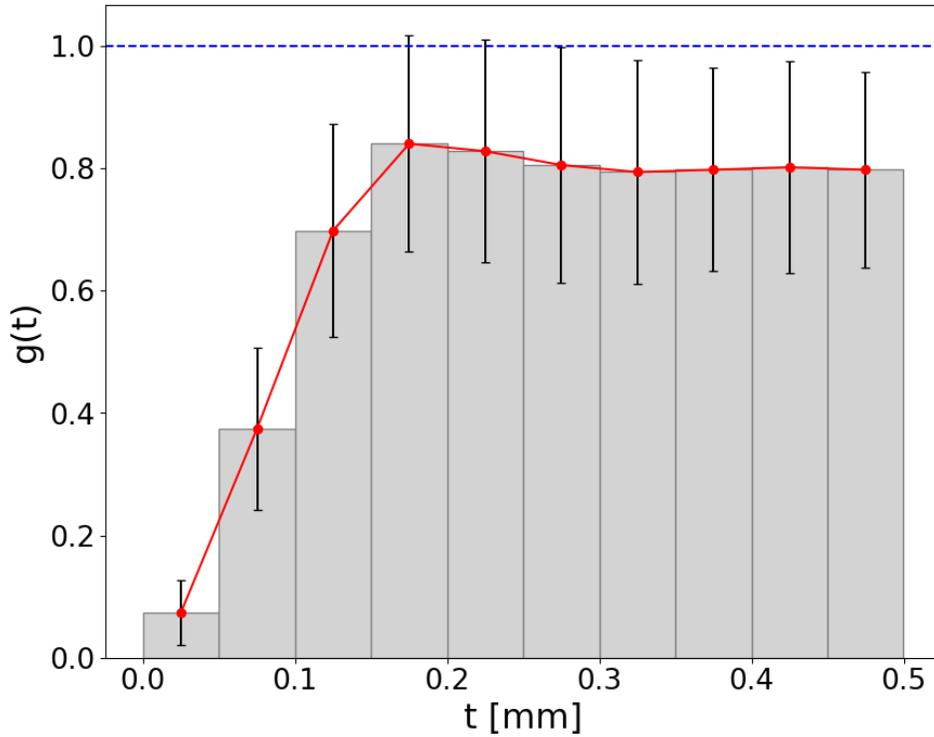
Fig. 3.11. The RDF calculated for one coarse aggregate and spherical sand particles with a slice density of 1.
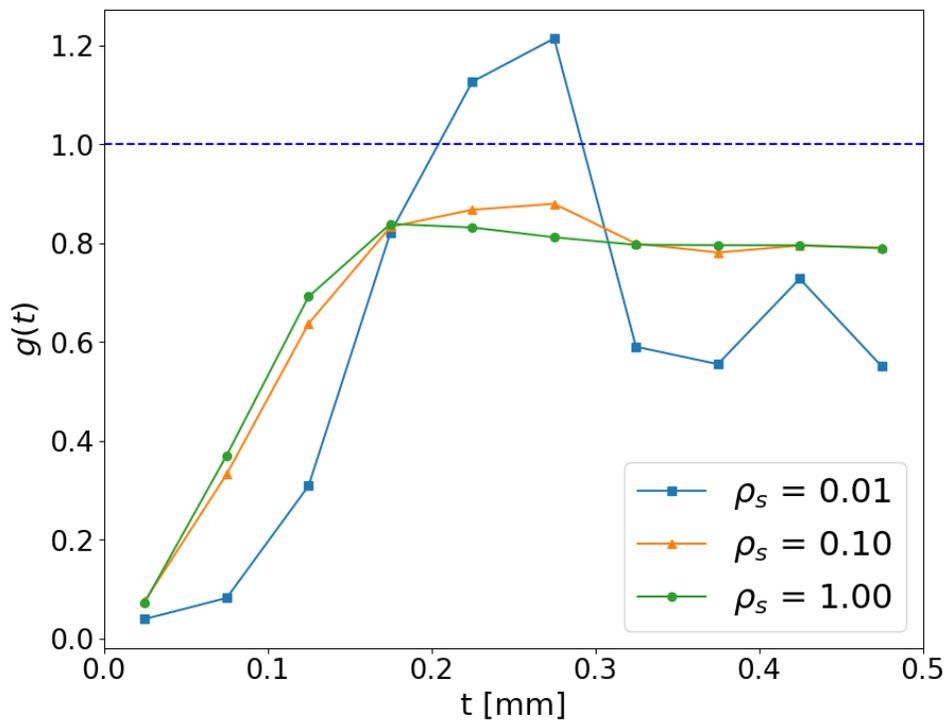
Fig. 3.12. The RDF calculated for one coarse aggregate with four different slice densities with spherical sand particles. Slice density of 1 corresponds to R_s of 0.05 mm/pixel.
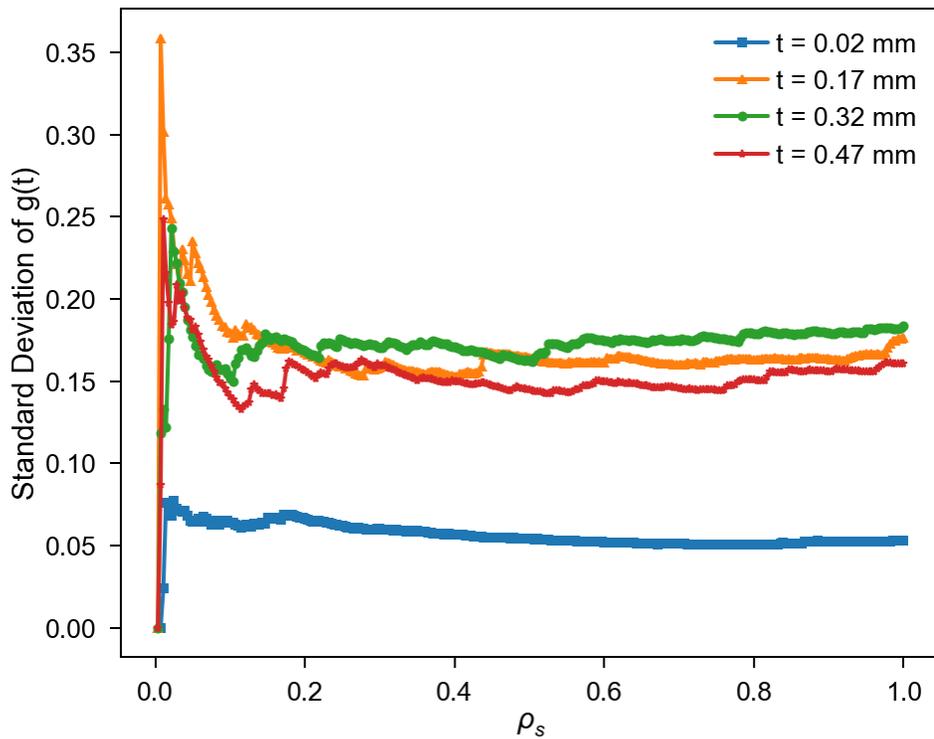
Fig. 3.13. **Variation in standard deviation of the RDF with increasing slice density(ρ_s). Four distances from the particle surface is considered. Slice density of 1 corresponds to R_s of 0.05 mm/pixel. The sand particles in sieve 3 is assumed to be spherical in shape.**

3.5 Summary

The impact of overlapping the uniform thickness shells is surprisingly broad and has given rise to many questions. A 2D slicing technique that leveraged the EOB idea previously developed for detecting overlap between two 3D particles has been implemented. This greatly eases the computational burden of the existing 3D visualization scheme when high density Anm models are generated and in some cases the 2D visualization has proved to be the only viable option. 2D slice images have been compared with their corresponding 3D models and interesting geometric effects such as apparent increase in uniform thickness shell, single particle appearing to be multiple particles and the occurrence of patches of the uniform thickness shell have led to the

conclusion that 2D slicing gives rise to features that are clearly understood only when the

3D structure is also visualized. This has been identified as a potential tool for guiding the

inference of features from sliced experimental samples. Finally, a method for

characterizing the wall effect observed in the Anm model was developed and preliminary

analysis of this system was performed.

3.6 References

Bentz, D. P., Garboczi, E. J. and Stutzman, P. E. (1993) 'Computer modelling of the
interfacial transition zone in concrete', Interfaces in cementitious composites.
Chapman & Hall/E&FN Spon, pp. 107–116.

Carey, R. and Bell, G. (1997) *The annotated VRML 2.0 reference manual*. Addison-
Wesley.

Crumbie, A. K. (1994). Characterisation of the microstructure of concrete. Imperial
College London (University of London).

Haecker, C., Garboczi, E. J., Bullard, J. W., Bohn, R. B., Sun, Z., Shah, S. P., & Voigt, T.
(2005). Modeling the linear elastic properties of Portland cement paste, 35, 1948–
1960. https://doi.org/10.1016/j.cemconres.2005.05.001

Scrivener, K. L., Crumbie, A. K. and Laugesen, P. (2004) 'The interfacial transition zone
(ITZ) between cement paste and aggregate in concrete', Interface Science, 12(4),
pp. 411–421. doi: 10.1023/B:INTS.0000042339.92990.4c.

Xu, W. X., Lv, Z. and Chen, H. S. (2013) 'Effects of particle size distribution, shape and
volume fraction of aggregates on the wall effect of concrete via random sequential
packing of polydispersed ellipsoidal particles', Physica A: Statistical Mechanics
and its Applications, 392(3), pp. 416–426. doi: 10.1016/j.physa.2012.09.014.

Zheng, J. jun, Wong, H. S. & Buenfeld, N. R. Assessing the influence of ITZ on the
steady-state chloride diffusivity of concrete using a numerical model. Cem.
Concr. Res. 39, 805–813 (2009).

CHAPTER FOUR: CONCLUSIONS

4.1 Innovative Contributions of this Research

The most important contributions of this research are (1) improving the Anm model's performance by integrating the EOB method for contact detection and the uniform thickness shell algorithm for irregular shaped particles, (2) introducing the 2D slicing feature for the Anm model, (3) combining the uniform thickness shell and the 2D slicing feature to develop a new framework to study the experimentally observed "wall effect" in concrete using the Anm model and (4) improving the computational performance of the Anm model code using shared memory parallelism. Furthermore, several opportunities for further research and development in this research has been identified. An illustration of the contributions of this research is presented in Fig. 4.1.
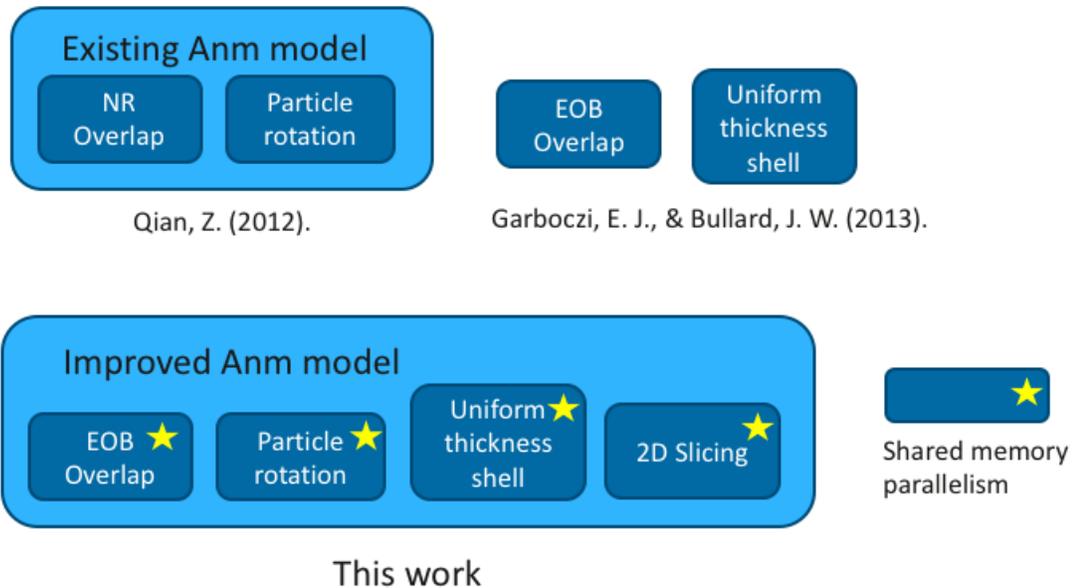
Fig. 4.1.   **Illustration of the contributions of this research to the Anm model.**

4.2 Summary and Outlook

The Anm model for modelling virtual concrete was improved and augmented by adding the following features:

(1) Integrating the EOB method for detecting overlap between star-shaped particles and comparing its performance with the previously used Newton-Raphson method.

(2) Adding the feature to add uniform thickness shells to individual particle shapes being parked in the Anm model and using it to control the minimum inter-particle distance. The effect of this feature on the overall packing density of the model was also studied.

(3) Identifying the computational bottlenecks in the Anm model code and introducing data parallelism so that the program can leverage the multiple cores available on most processors. The speedup achieved from this implementation was also studied.

(4) Modifying the particle packing algorithm and data visualization to efficiently generate a variation in the Anm model where particles do not overlap each other, but uniform thickness shells can overlap other shells as well as other particles.

(5) Developed a new feature for generating 2D slices from the 3D Anm model was developed.

(6) Utilized the 2D slicing method to quantify the wall effect observed in the Anm model using a radial distribution function.

These first three tasks were assimilated into one publication in a journal which is presented in Chapter 2. Tasks (4) to (6) were presented in Chapter 3.

The EOB method was found to be better than the Newton-Raphson method both in terms of computational efficiency as well as overlap detection accuracy. Even though the EOB method significantly improved the performance of particle parking, plenty of opportunity remains to further improve computational efficiency. The EOB method is currently restricted to checking if the particle being placed overlaps with one existing particle at a time. However, in dense packing scenarios, it must be computationally beneficial to concurrently check if the particle being parked has contact with multiple particles that are already parked in the vicinity. This parallel optimization opportunity is a potential candidate for data parallelism using libraries such as OpenMP. Other opportunities exist for task parallelism in the Anm model. For example, multiple particles can be attempted to park concurrently in different subdomains within the volume being packed. But packing multiple particles in parallel is a more complex task than detecting overlap of the newly placed particle with multiple already parked particles. The added complexity of parking multiple particles concurrently is partly because two concurrently parked particles have the potential to be overlapping even though they are placed in separate subdomains. This scenario happens when the two particles are being parked in adjacent subdomains. Furthermore, the particle being parked has the potential to be overlapping another already placed particle in the adjacent subdomain.

The ability to add uniform thickness shell to individual particles significantly increases the potential applications accessible to the Anm model. When the shells are assumed to be non-overlapping as demonstrated in this research, the uniform thickness shells become a means to controlling the minimum interparticle distance. The uniform thickness shell is not retained in the final model per this assumption. However, other

applications such as the ITZ layer model might require the uniform thickness shell to be overlapping other shells and particles. It has been identified that the Newton-Raphson iteration method used to solve system of equations for creating the uniform thickness shell fails to converge when the shell thickness is more than ~2%. This presents an opportunity to improve the numerical stability of the program.

The data parallelism implementation using the Microsoft PPL library has resulted in a speedup of ~5 and an efficiency of ~0.6. One disadvantage of the PPL library is that the program can only be compiled for Windows based operating systems. Other libraries such as OpenMP (Dagum and Menon, 1998) and Intel Threading Building Blocks (TBB) library (Willhalm and Popovici, 2008) which aim at providing shared-memory parallelism, also known as data parallelism can target Windows based OS's as well as Unix based OS's. Since most of the cluster computers accessible to universities are Unix based, implementing the parallelism using these libraries increases the accessibility of the Anm model in terms of the hardware capability. The libraries such as OpenMP and TBB provide the ability to distribute the load on multiple central processing units (CPU's). However, other libraries such as the CUDA Toolkit (Nvidia, 2010) can distribute the computational load to graphical processing units (GPU's) through shared-memory parallelism. Performing domain decomposition and parking the particles in subdomains in parallel has the potential to significantly improve the efficiency. This type of parallelism is called distributed-memory parallelism and involves significant amount of code change. The distributed memory parallelism can be implemented using API's that distribute the load on the CPU's or the API's that distribute the load on GPU's. The recommendations involving shared memory parallelization can be implemented with

minimal code change and provide the ability to utilize cluster computers. The

recommendations involving distributed memory parallelization can be highly beneficial

while trying to build models which contain large number of very small particles such as

cement particles or fine aggregates.

The 2D slicing feature is a useful tool to gain a perspective on the geometric

effect of irregular shapes when observed on a 2D surface. A typical example of the

geometric effect is where a single particle appears to be two separate particles when

viewed in 2D (Fig. 3.3). The process of analyzing material microstructural feature using

cross sections is a common practice in materials science. Tools such as Focused Ion

Beam (FIB) are routinely used to cut slices of materials to be observed under

microscopes. Much can be learned by carefully analyzing Anm model slices from

different types of packing fractions and aggregate types. The slice images can also be an

effective way to perform statistical analysis of packing densities and distributions as a

function of the Euclidian distance from the particle surfaces. An example of such an

analysis is presented in section 3.4 where the reduced packing density distribution near

the aggregate surface is quantified.

The current research exemplifies the use of the spherical harmonic expansion

method to represent irregular shapes in the context of concrete mesoscale microstructure

modelling. However, the applications of this technology are not limited to this material or

scale or even the domain of materials modelling. Other potential material models that can

use this idea could be the modelling of flow of red blood cells or macromolecules which

generally tend to arrange in arbitrary shapes and other systems where shape tends to play

in important role. Other domains that can benefit from this idea includes 3D data

visualization where large volumes of 3D data need to rendered. Since storage costs incurred by the current method are typically much lesser than voxel based representation of irregular shapes, this method has the potential to revolutionize 3D data storage and visualization demonstrating the broad impact of this research. The recent surge in the virtual reality and augmented reality further justifies the need for investing more resources in the field of 3D data and in this research topic.

REFERENCES

Dagum, L. and Menon, R. (1998) 'OpenMP: an industry standard API for shared-memory programming', *IEEE computational science and engineering*. IEEE, 5(1), pp. 46–55.

Nvidia, C. (2010) 'Programming guide'.

Willhalm, T. and Popovici, N. (2008) 'Putting intel® threading building blocks to work', in *Proceedings of the 1st international workshop on Multicore software engineering*. ACM, pp. 3–4.